Materials Science Under Extreme Conditions of Pressure and Strain Rate

B.A. REMINGTON, G. BAZAN, J. BELAK, E. BRINGA, M. CATURLA, J.D. COLVIN, M.J. EDWARDS, S.G. GLENDINNING, D.S. IVANOV, B. KAD, D.H. KALANTAR, M. KUMAR, B.F. LASINSKI, K.T. LORENZ, J.M. McNANEY, D.D. MEYERHOFER, M.A. MEYERS, S.M. POLLAINE, D. ROWLEY, M. SCHNEIDER, J.S. STÖLKEN, J.S. WARK, S.V. WEBER, W.G. WOLFER, B. YAAKOBI, and L.V. ZHIGILEI

Solid-state dynamics experiments at very high pressures and strain rates are becoming possible with high-power laser facilities, albeit over brief intervals of time and spatially small scales. To achieve extreme pressures in the solid state requires that the sample be kept cool, with $T_{sample} < T_{melt}$. To this end, a shockless, plasma-piston "drive" has been developed on the Omega laser, and a staged shock drive was demonstrated on the Nova laser. To characterize the drive, velocity interferometer measurements allow the high pressures of 10 to 200 GPa (0.1 to 2 Mbar) and strain rates of 10^6 to 10^8 s^{-1} to be determined. Solid-state strength in the sample is inferred at these high pressures using the Rayleigh-Taylor (RT) instability as a "diagnostic." Lattice response and phase can be inferred for single-crystal samples from time-resolved X-ray diffraction. Temperature and compression in polycrystalline samples can be deduced from extended X-ray absorption fine-structure (EXAFS) measurements. Deformation mechanisms and residual melt depth can be identified by examining recovered samples. We will briefly review this new area of laser-based materials-dynamics research, then present a path forward for carrying these solid-state experiments to much higher pressures, $P > 10^3$ GPa (10 Mbar), on the National Ignition Facility (NIF) laser at Lawrence Livermore National Laboratory.

I. INTRODUCTION

HIGH-STRAIN-RATE materials dynamics and solid-state deformation mechanisms have been a topic of great interest for decades.[1–8] Materials response to shocks and other high-strain-rate deformation has led to a number of theories, both empirical and, more recently, physically based. There is a particular interest in developing and testing constitutive models that allow continuum hydrodynamic computer codes to simulate plastic flow in the solid state. Models such as the Johnson–Cook,[9] Zerilli–Armstrong,[10,11] mechanical threshold stress (MTS),[12] thermal-activation–phonon-drag,[13,14] Steinberg–Lund,[15] and Steinberg–Guinan[16] models are widely used in the materials-dynamics community. These models have typically been tested and "calibrated" with experiments on Hopkinson bars, Taylor cylinders, and with high-explosive (HE)–driven shock or compression waves at pressures up to a few tens of gigapascals and strain rates of 10^3 to 10^5 s^{-1}. We describe here our progress toward developing experiments in a new regime of materials science at much higher pressures ($P \gg 10$ GPa) and strain rates ($d\varepsilon/dt \gg 10^5$ s^{-1}), where we anticipate new dynamics and, possibly, new mechanisms of solid-state deformation. To reach these very-high-pressure conditions in solids, we use large laser facilities to focus macroscopic quantities of energy into microscopic volumes, generating very-high-energy densities (E_{Laser}/Volume $\sim P$). The time sequence of the ensuring dynamics in the samples under study is characterized with a variety of time-resolved and time-integrated diagnostics.

To illustrate the potential for exploring new regimes of extreme materials science, we present a list of ten fundamental questions that may be addressed with experiments at ultrahigh pressures and strain rates.

1. Are there upper limits on the dislocation density (ρ_{disloc}) and dislocation multiplication rate ($d\rho_{disloc}/dt$) as strain rates are increased to extremely high values, where $d\varepsilon/dt \gg 10^5$ s^{-1}?
2. Is there a "relativistic" regime at the highest $d\varepsilon/dt$ value (*i.e.*, is there an absolute limit on dislocation velocity (u_{disloc})?
3. How much do initial conditions matter at ultrahigh shear stresses and compressions?
4. Is Schmid's law universally obeyed at extreme applied shear stresses and $d\varepsilon/dt$ in single crystals?
5. What is the dominant deformation mechanism at ultrahigh strain rates?
6. How does the Peierls–Nabarro stress scale to ultrahigh pressures?
7. Does material strength continue to scale with shear modulus as P and d´/dt increase to extreme values (i.e., is

B.A. REMINGTON, G. BAZAN, J. BELAK, E. BRINGA, J.D. COLVIN, M.J. EDWARDS, S.G. GLENDINNING, D.H. KALANTAR, M. KUMAR, B.F. LASINSKI, K.T. LORENZ, J.M. McNANEY, S.M. POLLAINE, D. ROWLEY, J.S. STÖLKEN, S.V. WEBER, and W.G. WOLFER are with the Lawrence Livermore National Laboratory, Livermore, CA. Contact e-mail: remington2@llnl.gov M. CATURLA is with the Department of Applied Physics, Alicante, Spain. D.S. IVANOV and L.V. ZHIGILEI are with the Department of Materials Science and Engineering, University of Virginia, Charlottesville, VA. B. KAD, M.A. MEYERS, and M. SCHNEIDER are with the Department of Mechanical and Aerospace Engineering, University of California, San Diego, CA. D.D. MEYERHOFER and B. YAAKOBI are with the Laboratory for Laser Energetics, Rochester, NY. J.S. WARK is with the Clarendon Laboratory, Department of Physics, University of Oxford, Oxford, United Kingdom.

This article is based on an invited presentation given in the symposium "Dynamic Deformation: Constitutive Modeling, Grain Size, and Other Effects: In Honor of Prof. Ronald W. Armstrong," March 2–6, 2003, at the 2003 TMS/ASM Annual Meeting, San Diego, California, under the auspices of the TMS/ASM Joint Mechanical Behavior of Materials Committee.

there any limit to how strong a material can be as pressure is increased "without bound")?
8. What is the time scale for solid-to-solid, solid-to-liquid, and liquid-to-solid phase transitions?
9. Does a natural length scale exist and have an effect in plastic flows at very high strain rates?
10. Are there novel states or phases of matter that can be accessed or created by the application of extreme pressures over ultrashort durations?

In this article, we give an overview of our work to create an ultrahigh pressure–strain rate deformation-dynamics testbed. Our article is organized as follows.

Constitutive models are discussed in Section II, and Section III contains a description of the experimental methods for creating these conditions of high pressures and strain rates in solid-state samples (*i.e.*, the "drive"). In Section IV, we describe the techniques developed to infer material strength at high pressure and strain rate, and in Section V, we discuss the development of recovery techniques to infer integral information such as the average strength, peak pressure, and how much of the sample melted on release. In Section VI, we present progress in developing lattice diagnostics such as diffraction and extended X-ray absorption fine-structure (EXAFS) measurements. We discuss the outlook for the future in Section VII.

II. CONSTITUTIVE MODELS

Constitutive models offer a convenient way for solid-state deformation dynamics to be included into continuum hydrodynamics codes for integrated simulations. At the high strain rates relevant to the work described in this article, thermal activation and dislocation glide along slip planes are believed to be the fundamental mechanisms underlying deformation.[3,13–15] Resistance to dislocation transport microscopically is then what is referred to as material strength macroscopically. In the thermal-activation regime, when a shear stress is applied, dislocations are assumed to be pinned against barriers, until a thermal fluctuation can assist them over the obstacle to glide to the next barrier. In this "jerky-glide" regime,[14] the strain rate is given by Orowan's equation, $\dot{\varepsilon} = \rho_m b \overline{u}$, where $\overline{u} = \lambda_b/(t_w + t_g)$ is the average dislocation velocity, λ_b is the average distance between barriers, t_w is the time spent waiting for a thermal assist, and t_g is the time interval to freely glide to the next barrier. When the dislocations are freely gliding between obstacles at a velocity of u_g, an equilibrium drag equation gives $\sigma \mathbf{b} = D u_g$, where $u_g = \lambda_\mathbf{b}/t_g$, σ is the applied deviatoric stress, **b** is the Burgers vector, and D is the phonon-drag coefficient. (Table I provides definitions of symbols.) The interval of time that a pinned dislocation spends waiting for a thermal assist (t_w) is described by an Arrhenius rate equation, $t_w = \nu_a^{-1} \exp(\Delta G/\mathrm{k}T)$, where ν_a is the dislocation-attempt frequency, ΔG is the activation energy required to surmount the barrier at a given applied shear stress (σ), and T is the lattice temperature. These equations can be combined to give the thermal-activation constitutive equation,

$$\dot{\varepsilon} = \frac{\rho_m \mathbf{b}^2}{\dfrac{\mathbf{b}}{\boldsymbol{\lambda}_\mathbf{b} \nu_a} \exp\left(\dfrac{\Delta G}{\mathrm{k}T}\right) + \dfrac{D}{\sigma}} \qquad [1a]$$

Table I. Key Symbols Used in the Description of Materials Science at Extreme Pressures and Strain Rates

σ	material strength or flow stress (GPa)
σ_P	height of the Peierls barrier (GPa)
ρ_m	mobile dislocation density (cm^{-2})
ε	strain (dimensionless)
$\dot{\varepsilon}$, $d\varepsilon/dt$	strain rate (s^{-1})
b	Burgers vector (Å)
$\overline{u}$, $<u>$	average dislocation velocity (μm/ns = km/s)
u_g	dislocation velocity in the freeing gliding regime, unimpeded by obstacles (μm/ns)
λ_b	average barrier or obstacle separation (μm)
D	phonon drag coefficient (MPa-s)
t_g	time interval for a dislocation to glide freely from one obstacle to the next (s)
t_w	time interval a dislocation spends waiting for a thermal assist over the barrier (s)
ΔG	activation energy required for a dislocation to surmount a barrier at a given applied shear stress, σ
F_0	activation energy for a dislocation to surmount the barrier at $T = 0$ K
ν_a	dislocation attempt frequency (*i.e.*, thermal vibration frequency) (s^{-1})
v	Debye frequency (s^{-1})
L	length of a dislocation segment (μm)
w	width of a pair of kinks at the critical separation (for stability) in a dislocation (μm)
a	separation between Peierls valleys (μm)
U_n	energy to nucleate a kink pair in a dislocation (eV)
U_k	energy to nucleate a single dislocation kink (eV)
ω_a	atomic vibration frequency (s^{-1})
Ω	atomic volume (Å^3)
T	temperature (eV or K)
P	pressure (GPa)
G	shear modulus (GPa)
ρ	mass density (g/cm^3)
$\eta = \rho/\rho_0$	compression (dimensionless)
E_L	laser energy (kJ)
I_L	laser intensity (W/cm^2)
ν_eff	effective lattice viscosity (cm^2/s)
γ	Rayleigh-Taylor instability growth rate (s^{-1})
A	Atwood number: $(\rho_2 - \rho_1)/(\rho_2 + \rho_1)$
k	$\mathrm{k} = 2\pi/\lambda$ = sinusoidal perturbation wave number ($\mu\mathrm{m}^{-1}$)
g	acceleration or effective gravity (μm/ns^2)
$\mu(k)$	absorption coefficient ($\mu\mathrm{m}^{-1}$)
$\chi(k)$	normalized absorption coefficient (dimensionless)

where

$$\Delta G = F_0 \left(1 - \left(\frac{\sigma}{\tau_\mathrm{MTS}}\right)^p\right)^q \qquad [1b]$$

Here, F_0 represents the energy required to push the dislocation over the barrier at $T = 0$ K, τ_MTS corresponds to the mechanical threshold stress (the stress at $T = 0$ K required to surmount the peak of the barrier), and p and q represent barrier-shape parameters.[3]

The previous discussion assumes rigid dislocations that are undistorted in surmounting a barrier. This assumption is not appropriate for the strong Peierls barriers, (σ_P) of a bcc lattice. In surmounting σ_P in a bcc lattice, the dislocation bows considerably, nucleating and propagating a pair of dislocation kinks. To describe this process, one again starts with an Arrhenius equation for the kink-pair nucleation

rate, $\nu_n \approx \frac{\nu \mathbf{b}}{w} \frac{L}{2w} e^{-U_n/\mathrm{k}T}$, where w corresponds to the width of the critical pair of kinks. Here, $\nu\mathbf{b}/w$ represents an approximate frequency of vibration of the dislocation, ν being the Debye frequency, and $L/2w$ is approximately the number of wave lengths along the dislocation line at which nucleation might occur.[2] Together with Orowan's equation for $\sigma < \sigma_P$ (*i.e.*, thermal-activation regime), and noting that the average velocity of a dislocation moving as a result of nucleation of pairs of kinks is $u_n \approx a\nu_n$, gives

$$\dot{\varepsilon} \approx \left(\frac{\rho_m a \mathbf{b}^2 L \nu}{2w^2}\right) e^{-(U_n/\mathrm{k}T)} \qquad [2a]$$

Here, a corresponds to the separation between Peierls valleys in the bcc lattice. A variation on this was proposed by Hoge–Mukherjee,[13] who generalized the equation to include the phonon-drag regime when $\sigma > \sigma_P$, giving

$$\dot{\varepsilon} = \frac{\rho_m \mathbf{b}^2}{\frac{2w^2}{La\nu} \exp\left(\frac{2U_\mathrm{k}}{\mathrm{k}T}\left(1 - \frac{\sigma}{\sigma_P}\right)^2\right) + \frac{D}{\sigma}} \qquad [2b]$$

where $2U_\mathrm{k}$ corresponds to the energy to form a pair of kinks in the dislocation segment.

The regimes we expect to access are at pressures and strain rates that are factors of 10 to 1000 higher than where constitutive equations such as Eq. [2b] have been reliably tested. Hence, precisely how Eq. [2b] scales with pressure and strain rate is a question central to our research. Following Frost and Ashby,[8] we will assume that the key physical components scale individually, according to $\sigma_P \propto G$, $U_\mathrm{k} \propto G\mathbf{b}^3$, and $\mathbf{b} \propto \eta^{-1/3}$, where $\eta = \rho/\rho_0$ represents compression (where ρ_0 and ρ represent the ambient and compressed densities). The phonon-drag coefficient, D, also scales with T and η, due to the lattice phonon density. Starting from $D \approx \mathrm{k}T/(\Omega\omega_a)$, where ω_a is the atomic frequency and Ω is the atomic volume,[3,14] we can write

$$\omega_a \sim \frac{u_\mathrm{thm}}{r_\mathrm{atom}} \sim \frac{T^{1/2}}{\Omega^{1/3}} = \frac{T^{1/2}}{(\Omega_0/\eta)^{1/3}} \sim \eta^{1/3} T^{1/2} \qquad [2c]$$

where u_thm is the thermal atomic velocity, r_atom is the radius of the atom, Ω_0 is the atomic volume at ambient conditions, and $\eta = \rho/\rho_0$. The scaling of D with temperature and compression, then, is given by[17]

$$D \sim \frac{T}{\Omega\omega_a} \sim \frac{T}{(\Omega_\mathrm{o}/\eta)\eta^{1/3}T^{1/2}} \sim \eta^{2/3} T^{1/2} \qquad [2d]$$

The density of phonon modes increases with both η and T, as does D. Hence, the resistance to dislocation motion and, therefore, strength, should increase with T in this regime, which is opposite to the dependence of strength with temperature in the thermal-activation regime. Two more sophisticated constitutive models based on thermal activation are the MTS model[12,18] and the PTW model.[19] The latter model claims to be applicable over 15 decades of strain rate (10^{-3} to 10^{12} s^{-1}) and would seem to be ideally suited for describing the laser-based, high-strain-rate experiments discussed here.

To illustrate the dynamics of the Hoge–Mukherjee[13] model (Eq. [2b]) more clearly, consider two regimes, $\sigma \leq \sigma_P$ and $\sigma > \sigma_P$. In the thermal-activation regime, ($\sigma \leq \sigma_P$), the effect of phonon drag is negligible. Setting $D \approx 0$, Eq. [2b] can be rearranged to give

$$\sigma \approx \sigma_P\left(1 - \left(\frac{\mathrm{k}T}{2U_\mathrm{k}}\right)^{1/2} (\ln \dot{\varepsilon}_0 - \ln \dot{\varepsilon})^{1/2}\right) \qquad [2e]$$

where $\dot{\varepsilon}_0 = \rho_m \mathbf{b}^2 La\nu/(2w^2)$ is assumed to be a constant. In this regime, the dominant effect on strength is through the Peierls stress (σ_P), and the strain rate enters only logarithmically. Furthermore, $\sigma_P \sim G$,[8] so material strength is expected to scale with the shear modulus and, hence, increase with pressure. Conversely, for $\sigma > \sigma_P$, the Arrhenius exponential portion to Eq. [2b] disappears, since now $t_w = 0$, leaving

$$\sigma \approx \frac{D}{\rho_m \mathbf{b}^2}\dot{\varepsilon} \qquad [2f]$$

In this regime, strength scales directly with the strain rate and drag coefficient and inversely with the mobile dislocation density (ρ_m). The scaling of Eq. [2f] in particular, the fact that σ increases without bound with increasing $\dot{\varepsilon}$, has been called into question on physical grounds by Steinberg *et al.*[16]

An alternate constitutive equation that explicitly includes pressure, temperature, and compression, proposed for extremely high strain rates, is the Steinberg–Guinan model.[16] The basis for this model is the assumption that above some critical strain rate ($\sim 10^5$ s^{-1}), all effects due to strain rate have saturated, and material strength becomes independent of strain rate. The only parameters that effect strength in this model are P, T, η, and strain (ε). The model is essentially a first-order Taylor expansion in pressure and temperature, with a work-hardening prefactor ($f(\varepsilon)$) and a small correction for compression,

$$\sigma = \sigma_0 f(\varepsilon)\left(1 + \left(\frac{G_P'}{G_0}\right)\frac{P}{\eta^{1/3}} + \left(\frac{G_T'}{G_0}\right)(T - 300)\right) \qquad [3a]$$

$$G = G_0\left(1 + \left(\frac{G_P'}{G_0}\right)\frac{P}{\eta^{1/3}} + \left(\frac{G_T'}{G_0}\right)(T - 300)\right) \qquad [3b]$$

$$f(\varepsilon) = (1 + \beta(\varepsilon_i + \varepsilon))^n \qquad [3c]$$

where σ_0 and G_0 are the ambient strength and shear modulus, $\eta = \rho/\rho_0$ is the compression, and $G_P' = \partial G/\partial P$ and $G_T' = \partial G/\partial \mathrm{T}$ are the partial derivatives of shear modulus with pressure and temperature, respectively. It is assumed that the rate of change of strength with P and T is the same as that of the shear modulus, an assumption that is unproven at extreme conditions, due to lack of controlled data.

The Steinberg–Lund model[15] is a combination of the two models just described and is written as

$$\sigma = \left(\sigma_T(\dot{\varepsilon}, T) + \sigma_A f(\varepsilon)\right)\frac{G(P,T)}{G_0} \qquad [4a]$$

where the thermally activated term, $\sigma_T(\dot{\varepsilon}, T)$, is determined by

$$\dot{\varepsilon} = \frac{1}{\frac{1}{C_1}\exp\left(\frac{2U_\mathrm{k}}{\mathrm{k}T}\left(1 - \frac{\sigma_T}{\sigma_P}\right)^2\right) + \frac{C_2}{\sigma_T}} \qquad [4b]$$

and is assumed applicable only when $\sigma \leq \sigma_P$. For $\sigma > \sigma_P$, Eq. [4a] becomes $\sigma \approx \sigma_A f(\varepsilon) G/G_0$, which is essentially Eq. [3a], the Steinberg–Guinan, $\dot{\varepsilon}$-independent model. Note that Eq. [4b] is identical to the Hoge–Mukherjee model (Eq. [2b]), provided that $C_1 = \rho_m L a \mathbf{b}^2 \nu/(2w^2) = \dot{\varepsilon}_0$ and $C_2 = D/(\rho_m \mathbf{b}^2)$. In Eq. [4], σ_A, C_1, U_k, σ_P, and C_2 are all assumed to be constants, and the scaling with P and T is taken into account with the G/G_0 overall factor in Eq. [4a].

To illustrate the mechanics of these models, we plot the results from the Hoge–Mukherjee model (Eq. [2b]) over a range of pressures in Figure 1(a) and of temperatures in Figure 1(b), assuming $\sigma_P \sim G$, $U_k \sim G\mathbf{b}^3$, $\mathbf{b} \sim \eta^{-1/3}$, and $D \sim \eta^{2/3} T^{1/2}$ scaling, and assuming that ρ_m, w, L, a, and ν are constant. The input-parameter set given for Ta in References 13 and 15 is used and reproduced in the figure caption. Figure 1(a) shows applied shear stress (strength) *vs* strain rate for pressures ranging from ambient to 500 GPa (5 Mbar), assuming the temperature is held fixed at room temperature. The thermal-activation region dominates at strain rates below $\sim 10^5$ s^{-1}, where $\sigma < \sigma_P$, and phonon drag dominates at $d\varepsilon/dt > 10^5$ s^{-1},

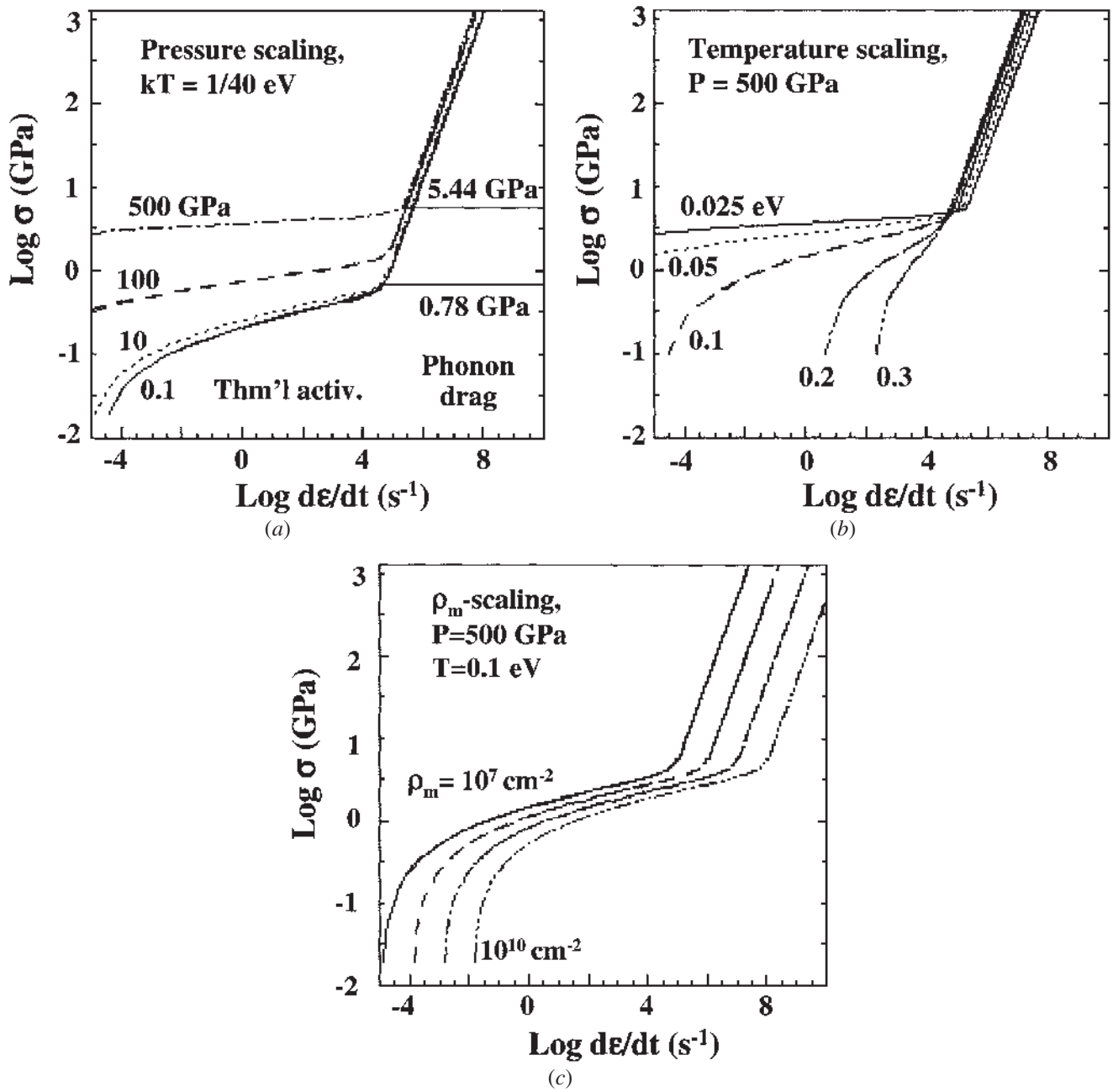

Fig. 1—Applied shear stress *vs* strain rate for the Hoge–Mukherjee thermal activation-phonon drag constitutive model for Ta.[13,15] The parameters used were taken from Refs. 13 and 15, and correspond to $a \approx b = 2.86$ Å, $L/b = 10^4$, $w/b = 24$, $U_k = 0.31$ eV, $D = 10^{-10}$ MPa·s, $\rho_m = 10^7$ cm^{-2}, $\nu = 10^{13}$ s^{-1}, and $\sigma_P = 1$ GPa. (*a*) Holding temperature fixed, scaling pressure over the range (bottom to top) 0.1, 10, 100, and 500 GPa. (*b*) Holding pressure fixed at 500 GPa, scaling temperature over the range (top to bottom) 0.025, 0.05, 0.1, 0.2, and 0.3 eV. (*c*) Holding pressure fixed at 500 GPa, and temperature fixed at 0.1 eV, scaling mobile dislocation density over the range (left to right) $\rho_m = 10^7$, 10^8, 10^9, and 10^{10} cm^{-2}, respectively.

where $\sigma > \sigma_P$. For comparison, the strain-rate-independent results from the Steinberg–Guinan model of strength (Eq. [3]) are shown by the horizontal lines, for $d\varepsilon/dt > 10^5\ s^{-1}$. The scaling of Hoge–Mukherjee strength with temperature over the range $kT = 1/4$ to 0.3 eV is shown in Figure 1(b). Note the strong drop in strength with temperature in the thermal-activation regime ($d\varepsilon/dt < 10^5\ s^{-1}$), whereas in the phonon-drag regime ($d\varepsilon/dt > 10^5\ s^{-1}$), the strength actually increases with increasing temperature. This is due to the increased resistance from dislocation-phonon scattering due to the higher phonon density at higher temperatures.[17] For example, in the thermal-activation regime at $d\varepsilon/dt \sim 10^3\ s^{-1}$, as T increases from 1/40 to 0.3 eV, strength decreases by a factor of ~6, whereas in the phonon-drag regime at $d\varepsilon/dt \sim 10^6\ s^{-1}$, the strength increases by a factor of ~3 for this increase of T. In Figure 1(c), the predicted variation of strength with dislocation density is shown over the range $\rho_m = 10^7$ to $10^{10}\ cm^{-2}$. The effect of higher dislocation densities is to translate the curves to the right-hand side (higher $\dot{\varepsilon}$), since, for all other parameters held fixed, $\dot{\varepsilon} \propto \rho_m$ (Eq. [2b]). The time-dependent mobile dislocation density at high strain rates is very uncertain; hence, so also is the point of transition from thermal activation to phonon drag. Note also that the Steinberg–Guinan strength is independent of dislocation density, the assumption being that at these high strain rates, ρ_m has saturated.

In summary, there is great uncertainty in the constitutive response of materials at $d\varepsilon/dt > 10^5\ s^{-1}$. Determining which model applies will require experimental data at these high strain rates. Measurements of strength even at the 30 to 50 pct level of accuracy could be helpful here to help establish which mechanism is at play in $\dot{\varepsilon} > 10^5\ s^{-1}$ deformations.

III. SHOCKLESS-DRIVE DEVELOPMENT

In this section, we show the results of two experimental techniques for generating a high-pressure "drive" to compress samples in the solid state at high strain rates. Each technique has been experimentally demonstrated at pressures up to ~10^2 GPa. Scaling simulations show that in future facilities, this technique should be able to drive samples in the solid state to much higher pressures ($P > 10^3$ GPa).

We show in Figure 2 the results from a new shockless drive[20] that has been developed on the Omega laser.[21] The target consists of a low-Z, low-density reservoir (either low-density carbon foam or solid-density plastic) of nominal thickness of 0.2 to 0.4 mm, followed by a 0.4 to 0.8 mm vacuum gap, then an Al sample, as illustrated in Figure 2(a). A laser pulse with an energy of 0.5 to 2.0 kJ in a temporally square pulse shape with a duration of 4 to 11 ns is used to drive a strong shock through the low-Z reservoir. When the shock reaches the back side (the side opposite where the laser was incident), the reservoir unloads into vacuum as a gas of "ejecta." The pressure that is applied to the sample results from the increasing ram pressure, $P_{ram} = \rho_{ejecta} v^2_{ejecta}$, which increases smoothly and monotonically in time as the reservoir unloads, until the reservoir material is depleted. This technique for generating shockless compression was modeled after the early work of Barnes using high-explosive (HE)–driven shock as the source of the shock in the reservoir.[22]

The pressure wave is measured with a line-velocity interferometer[23] viewing the back side of a 10 to 30 μm flat Al sample, an example image of which is shown in the inset of Figure 2(a). This particular shot used a 300-μm-thick carbonized resorcinol foam reservoir with a density of 100 mg/cm^3 with a 430 μm gap, and a 29.4 μm Al sample, was shot at a laser intensity of 5×10^{12} W/cm^2, and used 0.87 kJ of laser energy in a 3.7-ns-long square laser pulse.[20] The horizontal direction of the image in the inset is the "streak" or time direction, and the vertical direction corresponds to the transverse position along the sample. The interference fringes in the velocity-interferometer diagnostic are proportional to velocity, with each fringe shift δ, (marking a fringe position) corresponding to a known velocity increment, (δv). Thus, measuring the fringe shift vs time and position on the foil is a direct measure of the velocity of that location of the back side (free surface) of the foil, as shown by the curve labeled U_{FS} in Figure 2(b). There are no shock discontinuities observable in the $U_{FS}(t)$ trace, meaning that the rising pressure pulse is shockless. Using the standard hydrodynamic equations, with a known equation of state for Al, allows the free-surface velocity profiles to be backintegrated to infer the applied pressure *vs* time at the front surface of the Al sample,[24] as illustrated by the curve labeled "P" in Figure 2(b). The peak pressure in the sample is directly proportional to the shock pressure in the reservoir, P_{res}, which (based on numerical simulations) scales as $P_{sample} \propto P_{res} \propto \dfrac{\omega_L^{0.5} I_L^{0.76}}{t_L^{0.13}}$. Here ω_L, I_L and t_L correspond to the laser frequency, intensity (W/cm^2), and laser pulse length, respectively, for an experiment optimally designed for maximum pressure and rise time.[20] This scaling can be expressed in terms of total laser energy, E_L, by noting that $I_L \propto \dfrac{E_L}{\phi_L^2 t_L}$ and for an optimized design $\phi_L \propto L_{res} \propto v_{shk}\, t_L \propto \left(\dfrac{P_{res}}{\rho_0}\right)^{1/2} t_L$, where ϕ, L_{res}, v_{shk}, and ρ_0 correspond to laser spot size, reservoir thickness, shock velocity, and initial density in the reservoir, respectively. Combining these three relations gives

$$P_{sample} \propto \frac{(\rho_0 E_L)^{0.43}}{t_L^{1.37}} \left(\frac{\omega_L}{3}\right)^{0.28} \qquad [5]$$

This shows that to achieve higher pressures requires increasing E_L (at a given t_L) or decreasing t_L (at a given E_L), both of which increase the laser intensity and, hence, shock pressure in the reservoir. The disadvantage of decreasing t_L, which increases I_L, is that the pressure pulse steepens more rapidly into a shock wave at high pressure, possibly melting or vaporizing the target, and the strain rate increases.

This backintegration analysis technique exhibits some sensitivity to the material strength of the sample. To illustrate this, we assume the pressure *vs* time shown by the curve labeled P in Figure 2(b), then apply this in the "forward" direction with a hydrodynamics code (CALE), varying the assumed material strength of the Al sample, as shown in Figure 2(c). Assuming no strength ($\sigma = 0$) leads to the dashed curve. The temporal modulations result from the fact that the Al sample was moderately thin (29.4 μm). When the compression wave first reaches the back side of the foil, the applied pressure is still rising on the front side of the foil. This leads to the compression-wave reverberation observed

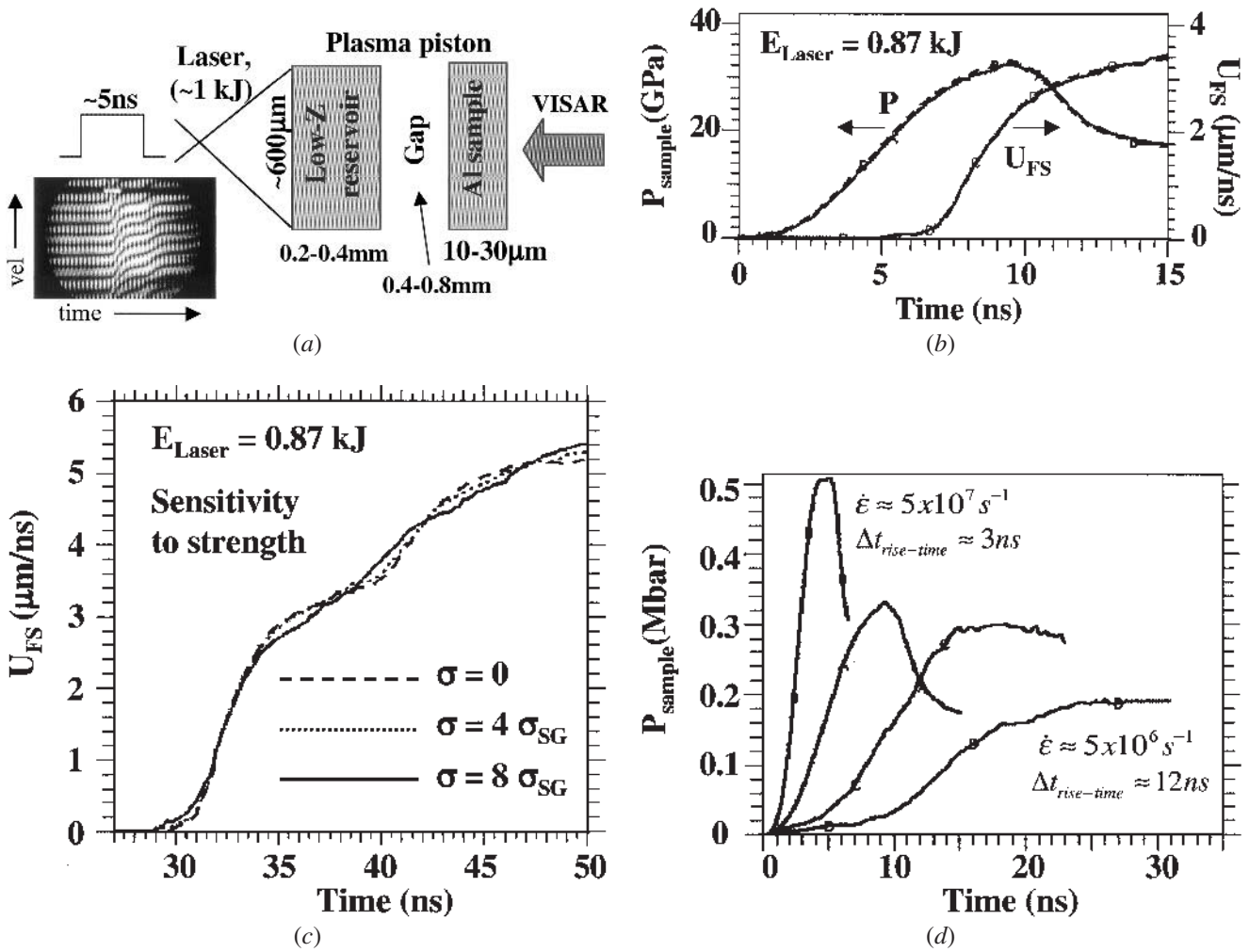

Fig. 2—(*a*) Configuration for the laser-driven shockless compression drive. The inset shows a "raw" velocity interferometer trace, where the diagnostic is viewing the back surface of a 29-μm-thick Al sample compressed with this shockless drive. (*b*) Free surface velocity history (curve labeled U_{FS}) measured with the velocity interferometer off the back surface of the Al sample, and inferred pressure on the front surface of the Al (curve labeled P) using a "back integration" analysis technique.[24] The time $t = 0$ here corresponds to when the applied pressure on the front of the Al sample begins. (*c*) Similar to (*b*) only plotted over a longer time interval for these same data, and adjusted so that $t = 0$ corresponds to when the laser is first incident on the reservoir. The dashed curve assumes no material strength in the Al sample ($\sigma = 0$), whereas the dotted and solid curves assume strengths of $\sigma = 4\sigma_{SG}$ and $8\sigma_{SG}$, respectively. As the strength of the sample is increased, the degree of the modulations in time is softened or smoothed out, due to the damping caused by the reverberating compression waves doing work against the strength of the sample. This work goes irreversibly into heat in the sample. (*d*) Pressure histories measured for four different laser shots on the Omega laser, spanning peak pressures ranging from 20 to 50 GPa, and corresponding strain rates of 5×10^6 s^{-1} to 5×10^7 s^{-1}.[20]

in the simulation (Figure 2(c)) and in the data (inset of Figure 2(a)). The effect of material strength in the sample tends to smooth out these reverberations, because each compression wave does work against the strength of the sample, which generates heat, thus, damping out the waves. If we assume nominal Steinberg–Guinan strength (not shown), the result would be essentially indistinguishable from the $\sigma = 0$ case, suggesting that this damping effect is predicted to be rather weak. Even if the strength were 4 times larger than the nominal Steinberg–Guinan strength ($\sigma = 4\sigma_{SG}$), shown by the dotted curve in Figure 2(c), the damping effect would still be very small, and probably not observable. Increasing the assumed strength in this one-dimensional (1-D) simulation to 8 times the Steinberg–Guinan strength ($\sigma = 8\sigma_{SG}$) finally does produce an observable damping effect, as shown by the solid curve in Figure 2(c). This raises an intriguing possibility. In the strength experiments being designed for the National Ignition Facility (NIF) laser[25,26] at pressures in excess of 10^3 GPa, the strength is predicted to increase significantly, by factors of 10 or more, due to pressure hardening in some metals. The damping out of reverberations in velocity-interfeometer measurements may allow the strength of the sample at very high pressures to be inferred.

The results of a series of experiments done with Al samples 15 to 30-μm-thick on the Omega laser, spanning peak strain rates of 5×10^6 to 5×10^7 s^{-1}, are illustrated in Figure 2(d). As the peak pressure increases from ~15 to ~50 GPa, the rise time of the pressure pulse decreases from ~12 to ~3 ns; hence, the strain rate of the sample increases. If these pulses were to traverse thicker samples, the pressure wave would steepen into a shock with a rise time of $\Delta t_{\text{rise time}} < 1$ ns, as verified by separate experiments (not shown). The strain rate in the sample depends on three factors: (1) the sound speed in the reservoir at shock breakout, which determines how rapidly the reservoir unloads; (2) the gap size, which determines how spread out in time the

unloading ejecta becomes; and (3) the compressibility of the sample, which determines its compressional strain. To see how $\dot{\varepsilon}$ varies with these parameters, we do the following approximate analysis. Assume a polytropic equation of state (EOS) for the sample, $P \sim \rho^n$, *i.e.*, $\rho \sim p^{1/n}$. Then, $\dot{\varepsilon} \approx 1/3 \times \dot{\rho}/\rho \propto 1/\mathrm{n} \times \dot{p}/p$. But, $(\dot{p}/p)^{-1} \approx \delta t_p \approx L/C_s$ is a characteristic time scale over which pressure changes occur and should be proportional to the pressure-rise time. So, the strain rate varies as $\dot{\varepsilon} \propto C_s/nL$. Here, the n in the denominator represents the compressibility of the sample. A smaller n value means greater compression and, hence, greater strain over the same time interval, or a greater strain rate. The L in the denominator represents the gap size. A large L value spreads out the reservoir ejecta in time, slowing down the pressure-rise time, hence, lowering the sample strain rate. The C_s in the numerator represents the sound speed in the shock-compressed reservoir, $c_s \approx \left(\frac{P_{\mathrm{shk}}}{\rho^*_{\mathrm{res}}}\right)^{1/2}$. The strain rate goes up, therefore, with a stronger shock or lower density in the reservoir. Combining gives $\dot{\varepsilon} \propto \frac{1}{nL}\left(\frac{P_{\mathrm{shk}}}{\rho^*_{\mathrm{res}}}\right)^{1/2}$. By varying the laser intensity (which determines P_{shk} in the reservoir), initial reservoir density, and gap size in the experiments on the Omega laser, a factor-of-~20 span in pressure and strain rate, (10 to 200 GPa, 5×10^6 to $1 \times 10^8\ \mathrm{s}^{-1}$) has been achieved with this shockless drive. Also, apart from a thin surface layer on the drive side, the sample compression is nearly isentropic, since there is no shock.[27].

In Figure 3 an alternate approach, using staged shocks to achieve high pressures and strain rates in the solid state, is illustrated. In this experiment, done on the Nova laser, ~14 kJ of laser energy was focused into a ~5 × 3 mm Au cylindrical radiation cavity (hohlraum) to create a Planckian radiation drive, as illustrated in Figure 3(a).[28,29,30] The sample was mounted over a hole in the wall of the hohlraum at the midplane. The 20 μm Al sample ($\rho_{0,\mathrm{Al}} = 2.7\ \mathrm{g/cm^3}$) was mounted behind 20 μm of CH(2 pct Br) ablator ($\rho_{0,\mathrm{CH(Br)}} = 1.2\ \mathrm{g/cm^3}$), which converted the radiation flux into ablation pressure. The laser-power history is shown in Figure 3(b) and corresponds to a 0.8 TW, 4-ns "foot," followed by an intermediate step, then a peak of ~3 TW for a duration of 3 ns. Simulated temporal profiles for density, pressure, temperature, and melt temperature in the Al near the CH(Br)/Al

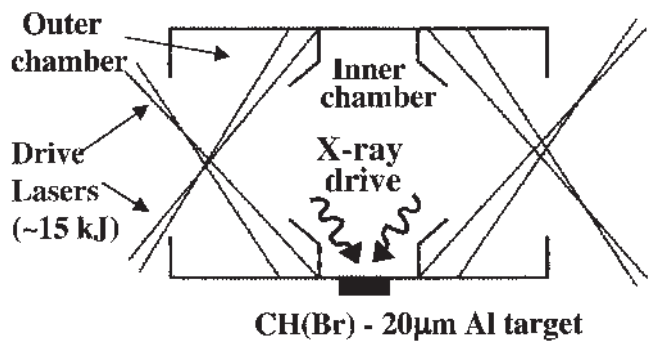

(*a*)

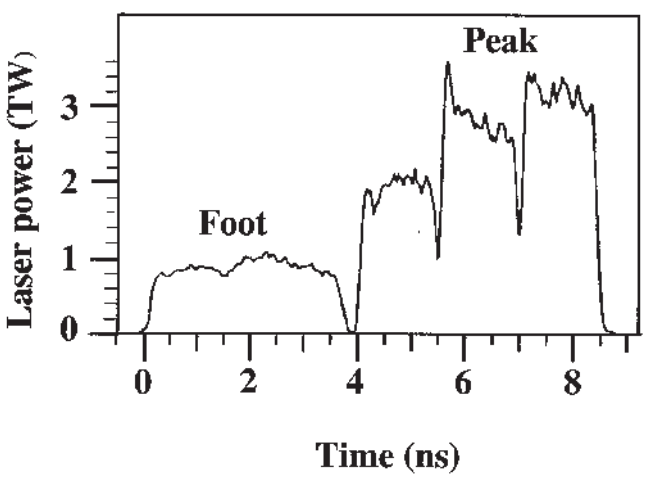

(*b*)

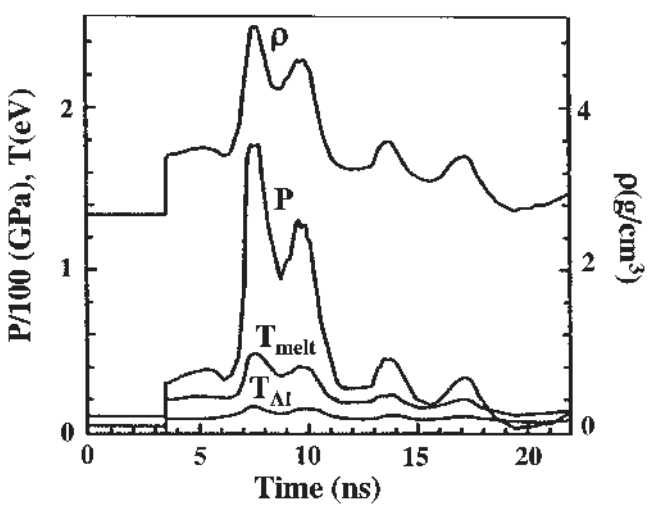

(*c*)

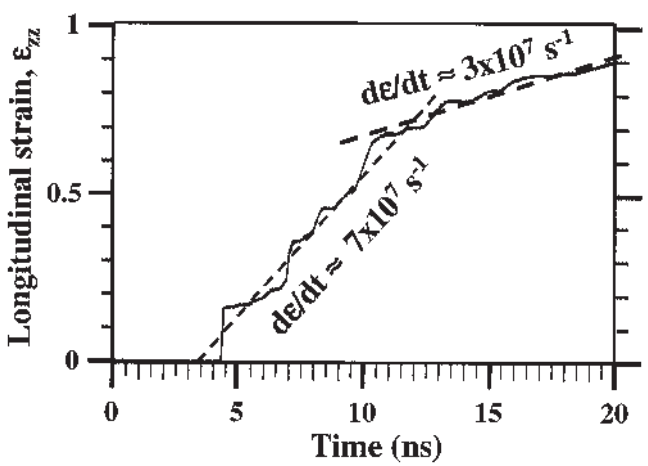

(*d*)

Fig. 3—(*a*) Configuration for a radiation driven, staged-shock compression of a CH(2 pct Br)-A16061 target, using the Nova laser. (*b*) The required laser power *vs* time, showing a foot, intermediate step, and peak. (*c*) The corresponding density, pressure, melt temperature, and temperature *vs* time in the Al sample from a 1-D LASNEX simulation for this staged-shock drive. (*d*) The corresponding strain *vs* time, showing the shocks and reverberations. Smooth fits show an average strain rate of $7 \times 10^7\ \mathrm{s}^{-1}$ early in the drive, dropping to $3 \times 10^7\ \mathrm{s}^{-1}$ later.[29]

interface are shown in Figure 3(c). The foot in the laser pulse launches an initial 30 GPa shock that generates an ~25 pct compression wave in the Al, followed by a second shock driven by the peak of the drive, reaching 160 GPa, at a peak compression of $\rho/\rho_0 \sim 1.8$. The laser pulse turns off at 8.5 ns, after which the pressure in the Al decays away in a series of reverberation waves. The resulting strain *vs* time in the Al from the simulations is shown in Figure 3(d), reaching a maximum of 0.9 by 20 ns. During the peak of the drive, the average strain rate from a straight-line fit was about $7 \times 10^7\ s^{-1}$, falling to about $3 \times 10^7\ s^{-1}$ later in the drive. This experiment was done on the Nova laser, which has since been shut down and dismantled.

IV. MATERIAL STRENGTH AT HIGH PRESSURE AND STRAIN RATE

To dynamically infer material strength, hydrodynamic instability experiments have been developed,[28,29,30] following the technique demonstrated in the early work by Barnes *et al*.[22] By accelerating a metal sample or payload with a lower-density, higher-pressure "pusher," a situation is created where the interface is hydrodynamically unstable to the Rayleigh–Taylor (RT) instability. Any pre-existing perturbations will attempt to grow, whereas material strength will act to counter or slow this growth. Therefore, by measuring the RT growth of machined sinusoidal ripples in metal foils that are accelerated by the drive and comparing the observed perturbation growth with that expected for an equivalent liquid target, the material strength at high pressures and strain rates may be inferred. We have derived an analytic result to illustrate how RT experiments can be used to infer material strength. Starting from the linear theory for RT growth of a layer of fluid of given thickness (h), viscosity (ν), and surface tension (T),[31] we replace the surface tension with G/k,[30] and then define an effective lattice viscosity as $\nu_{\text{eff}} = \sigma/6^{1/2}\,\rho\dot{\epsilon}$. This leads to a RT dispersion curve of the form

$$\gamma^2 + 2k^2\nu_{\text{eff}}\gamma + k \times \tanh(kh) \times (kG/\rho - Ag) = 0 \quad [6a]$$

where γ is the RT growth rate; that is, perturbations of an initial amplitude of δa_0 and wave number of $k = 2\pi/\lambda$ grow at $\delta a(t) = \delta a_0 e^{\gamma t}$. Here, the Atwood number at the interface is $A = (\rho_{\text{Al}} - \rho_{\text{CH(Br}_2)})/(\rho_{\text{Al}} + \rho_{\text{CH(Br)}})$ and g is the layer acceleration. This has the solution

$$\gamma = v_{\text{eff}}\,k^2\left(\left(1 - \left(\frac{C}{v_{\text{eff}}^2\,k^3}\right)\right)^{1/2} - 1\right) \quad [6b]$$

where $C = \tanh(kh) \times (kG/\rho - Ag)$. Notice, in the limit that $v_{\text{eff}} = 0$ and $G = 0$ (the classical result for incompressible, inviscid fluids), $\gamma^2 = Akg$ is recovered. In the elastic regime, the perturbation growth is reversible, and $v_{\text{eff}} = 0$, but G is finite. In the plastic-flow regime, $G = 0$, but v_{eff} corresponds to the effective lattice viscosity given previously, and the RT-induced deformation is irreversible. Note that a high material strength or low strain rate correlate with high lattice viscosity, which lowers the RT growth rate. Conversely, if the RT growth and $\dot{\varepsilon} \approx d/dt(2\delta a)1/(\lambda/2) = 4\delta\dot{a}/\lambda$ are measured, then average material strength at high pressure can be inferred by the previous equations.

One technique to dynamically measure the growth of ripples is with time-resolved face-on radiography. Consider, for example, the experimental configuration shown in Figure 3(a). The metal samples of Al6061 were machined with sinusoidal ripples with wave lengths of 10, 20, and 50 μm and peak-to-valley heights of 1 μm, then were thermally press fitted onto CH(Br) ablators. Each target package is mounted over a hole in the wall of the radiation cavity (hohlraum). The radiation deposits its energy in the CH(Br) at the ablation front, generating an ablation pressure which pushes on the higher-density Al sample, causing it to accelerate. In the accelerating reference frame of the interface, the higher-density Al is "sitting on top of" the lower-density CH(Br) fluid, a configuration which is hydrodynamically unstable due to the Rayleigh-Taylor (RT) instability. The tips of the ripples of Al will try to "sink to the bottom," causing the ripple amplitude to grow. Additional laser beams are delayed by 10 to 21 ns and focused onto a Sc disk, creating a burst of 4.3 keV He-α X-rays. These hard X-rays penetrate the foil in-flight and are recorded in a gated X-ray pinhole camera.[32] As the perturbations at the CH(Br)/Al interface grow due to the RT instability, the differential absorption (contrast) of the "backlighter" X-rays is increased. The thick regions of the Al absorb more than the thin regions, so the growing ripples can be measured with good spatial (<10 μm) and time ($<$ 1/2 ns) resolution. An example of such an in-flight radiograph is shown in Figure 4(a), from an experiment driven with the hohlraum drive shown in Figure 3.[29] The target was 20 μm CH(2 pct Br) backed by 20 μm Al6061-T6. The dark vertical stripes shown in the radiograph in Figure 4(a) correspond to the peaks of the ripples (the RT "spikes"), and the bright (white) regions correspond to the valleys (the RT "bubbles"). From analysis of a series of such laser shots done on the Nova laser, perturbation growth factor *vs* time was determined for the three wave lengths measured, as shown in Figures 4(b) through (d). The squares and the circles correspond to the same data, only analyzed in two different ways. Each represents the average over several (five to 15) independent data points under nominally identical conditions, and each individual datum was assigned an error bar. The squares are a weighted average of the individual points, and the error represents the statistical error of the mean. The circles result if each individual data point is given equal statistical weight, and the error bars now represent the standard deviation of the full distribution that went into the average. This latter representation reflects the level of scatter present in the individual data points.[29]

The curves represent two-dimensional (2-D) simulations with the code LASNEX, using the Steinberg–Guinan constitutive model[16] (Eq. [3]). In all cases, the curves represent simulated face-on radiographs, including the experimental resolution function, and analyzed for growth factor of the Fourier fundamental mode of contrast, in the same manner as the data. The dotted curves assume that the Al was liquid, that is, the material strength in the Al was set to $\sigma = 0$. The solid curve represents the result if $\sigma = \sigma_{SG}$ throughout the simulation, that is, if nominal Steinberg–Guinan strength were used. Looking at all three ripple wave lengths, we conclude that neither of these two calculations satisfactorily reproduces all of the data. The calculation using the nominal Steinberg–Guinan model underpredicts the growth of the 10-μm ripple throughout, underpredicts the growth of the

20-μm ripple early in time (16 ns), and slightly overpredicts the growth of the 50-μm rippled data late in time (21 ns). The liquid calculation ($\sigma = 0$ throughout) overpredicts the late-time data for all three wave lengths, with the discrepancy being the most severe for the 10 and 20 μm ripples. To gain some insight, additional simulations were done with $\sigma = 0$ for $t < 13$ ns, then with $\sigma = \sigma_{SG}$ thereafter. These simulations (not shown) were very similar to the $\sigma = 0$ (liquid) simulations shown by the dotted curves. The strength required to stop material from flowing once the perturbation has grown by a factor of ~10 and acquired finite flow velocities is significantly greater than that predicted by the nominal Steinberg–Guinan model. The dotted-dashed curves correspond to simulations with $\sigma = 0$ for $t < 13$ ns, then with $\sigma = G_{SG}/10 \approx 5\sigma_{SG}$ thereafter. The motivation for setting $\sigma = G_{SG}/10$ was to see the effect of setting the strength to be that of an ideal crystal (no dislocations) within the

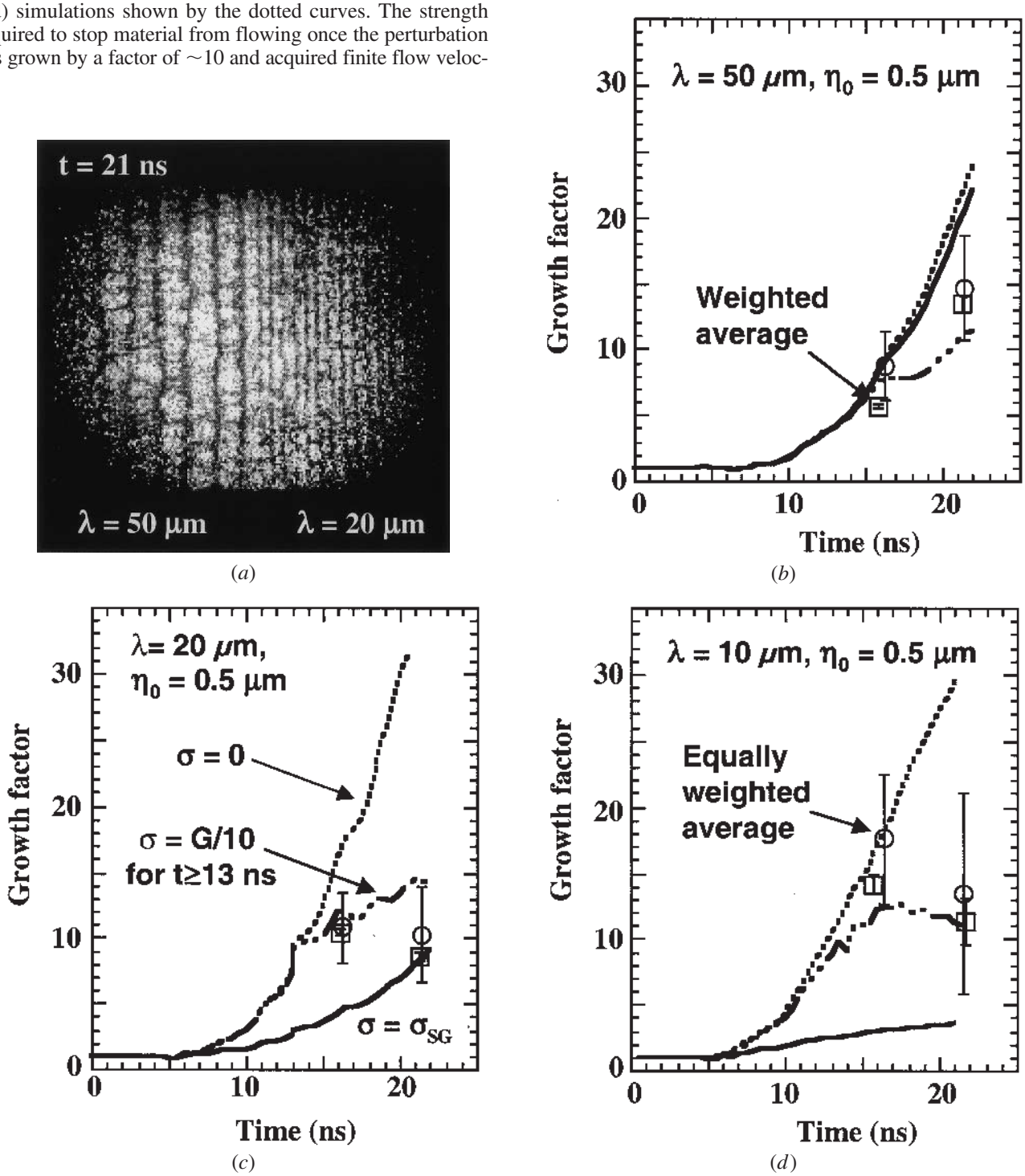

Fig. 4—(*a*) In-flight radiograph of a solid-state Rayleigh-Taylor (RT) experiment using thin foils of A16061. (*b*) through (*d*) Perturbation growth factors *vs* time for preimposed wavelengths of $\lambda =$ (*b*) 50 μm, (*c*) 20 μm, and (*d*) 10 μm, and initial amplitudes of $\eta_0 = 0.5$ μm for each. The upper dotted curves correspond to 2-D LASNEX simulations, assuming that the Al was liquid (strength $\sigma = 0$). The solid curves assume Steinberg–Guinan strength ($\sigma = \sigma_{SG}$) throughout the simulation. The dot-dashed curves assumed $\sigma = 0$ for $t < 13$ ns and $\sigma = G_{SG}/10$ for $t > 13$ ns.[29]

Steinberg–Guinan model at $t > 13$ ns. Interestingly, this *ad hoc* model does better reproduce the trends of the data. In the 13 to 17-ns time interval, this flow stress ($G_{SG}/10$) is approximately $\sigma \approx 5$ GPa.

The conclusion ($\sigma \approx 0$ early in time and $\sigma \approx 5$ GPa later in time) may be more significant than whether or not the Steinberg–Guinan model is right or wrong. We consider what such a large flow stress would imply within the Hoge–Mukherjee model.[13] The high strain rates (several times 10^7 s^{-1}) would imply that the deformation falls within the phonon-drag regime (Figure 1); hence, from Eq. [2f], we write $\sigma \approx D\dot{\varepsilon}/(\rho_m \mathbf{b}^2)$. If we take $D = 5 \times 10^{-3}$ dyne.s/cm^2 and $\mathbf{b} = 2.86$ Å for Al6061[33,34] and assume $D \sim \eta^{2/3} T^{1/2}$ (Eq. [2d]) and $\mathbf{b} \sim \eta^{-1/3}$ scaling, where $\eta = \rho/\rho_0$ is the compression, then $\sigma \approx$ 5 GPa implies $\rho_m = 9 \times 10^9 \approx 10^{10}$ cm^{-2}. This value for mobile dislocation density is significantly larger than the 3×10^7 cm^{-2} value deduced in Reference 33 in a strain-rate-independent analysis of their wave-profile data in Al6061 at $P_{max} \sim 2$ GPa. But, $\rho_m \approx 10^{10}$ cm^{-2} is comparable to the experimental values quoted for residual dislocation densities in shocked Cu at $P_{shk} = 20$ to 40 GPa.[35,36] Therefore, in the context of the phonon-drag model, a flow stress of 5 GPa at strain rates of several times 10^7 s^{-1} is not unphysically large. Whether or not this model and analysis really apply will require further experimental data in a similar regime.

Close examination of the radiograph shown in Figure 4(a) shows a random three-dimensional (3-D) structure superposed on the 2-D single-mode sinusoidal ripples. We consider whether this 3-D random structure could be related to the initial grain structure, shown in a face-on view in Figure 5(a). The grains in the face-on view had sizes of 10 to 50 μm, that is, the same size as the wave lengths of the preimposed ripples whose RT growth we are measuring. The foils were rolled to 20-μm thick, and, in this thin (axial) direction, the grains were severely flattened to 1 to 2 μm in thickness. To access whether the random 3-D pattern observed is grain related, we did the following analysis. In Fourier space, the

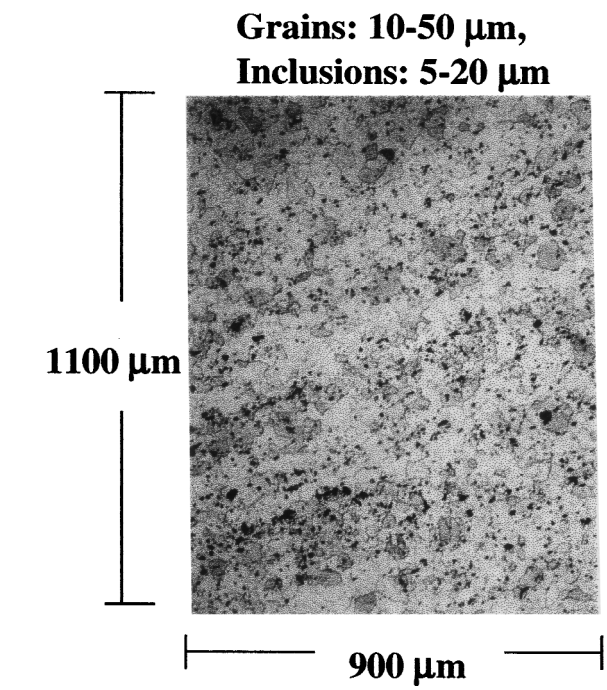

(*a*)

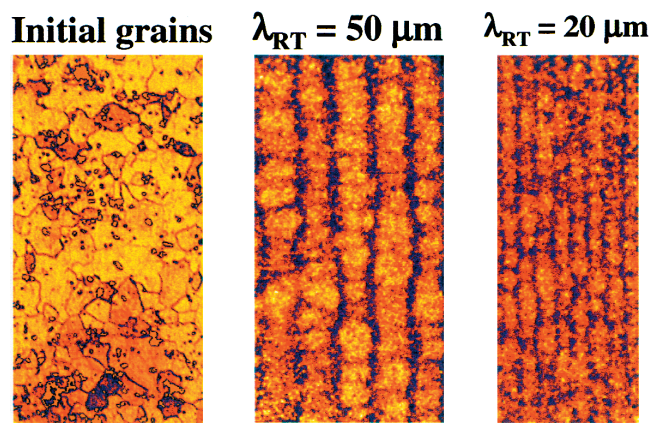

(*b*)

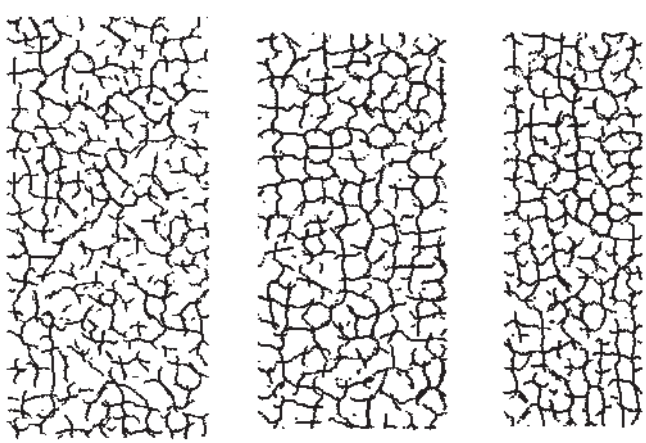

(*c*)

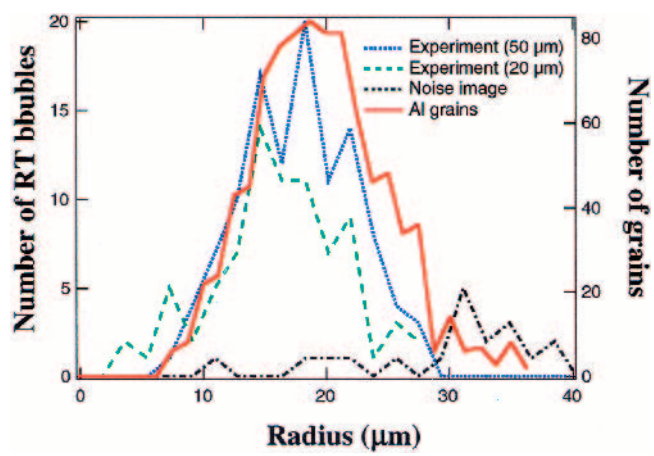

(*d*)

Fig. 5—(*a*) Initial grain structure (face-on view). (*b*) Initial grain structure (left), and inflight radiographs (middle, $\lambda = 50$ μm, and right, $\lambda = 20$ μm) from the Rayleigh–Taylor experiment. (*c*) Pattern corresponding to the initial grain structure (left) *vs* the patterns observed on the in-flight radiographs (middle, $\lambda = 50$ μm and right, $\lambda = 20$ μm). (*d*) Power spectra of the set of three patterns shown in Fig. 5(c).

2-D sinusoidal ripples were removed, then, in physical space, the remaining structure was analyzed with a pattern-recognition algorithm, as shown in Figures 5(b) and (c). Qualitatively, all three patterns shown in Figure 5(c) look rather similar. To quantify this comparison, the power spectra of these patterns are shown in Figure 5(d). The correlation between the random structure in the in-flight radiographs with the initial grain structure is not perfect, but close enough to motivate asking what affect the grains might have in this experiment.

Examination of Figure 3(c) shows that the Al6061 foil experienced a 30 GPa shock followed by a 160 GPa shock. We carried out molecular-dynamics (MD) simulations to examine the effects of shocks on grain boundaries. The MD code used was modified to include the effects of electron-phonon coupling and electron heat conduction, and we refer to this version of the code as molecular dynamics combined with the two-temperature model (TTM-MD).[37,38] Simulations were also done with the electron-phonon coupling and electron heat conduction turned off for comparison, and we refer to these simulations as just MD.

We show in Figure 6 the results of these simulations for shock-wave heating of a tilt grain boundary (GB) in an Al bicrystal.[37] The simulations were performed for a 30 GPa shock wave propagating through an Al bicrystal containing a single (110) Σ5 tilt GB. This particular GB had a density ~25 pct lower than the bulk material. The initial setup for the simulation was an fcc bicrystal with dimensions of 9.17 × 12.3 × 21.8 nm, periodic boundary conditions in the directions parallel to the shock front, and a GB located in the middle of the computational cell. Interatomic interaction is described by the embedded-atom method in the form and parameterization suggested in Reference 39. The parameters

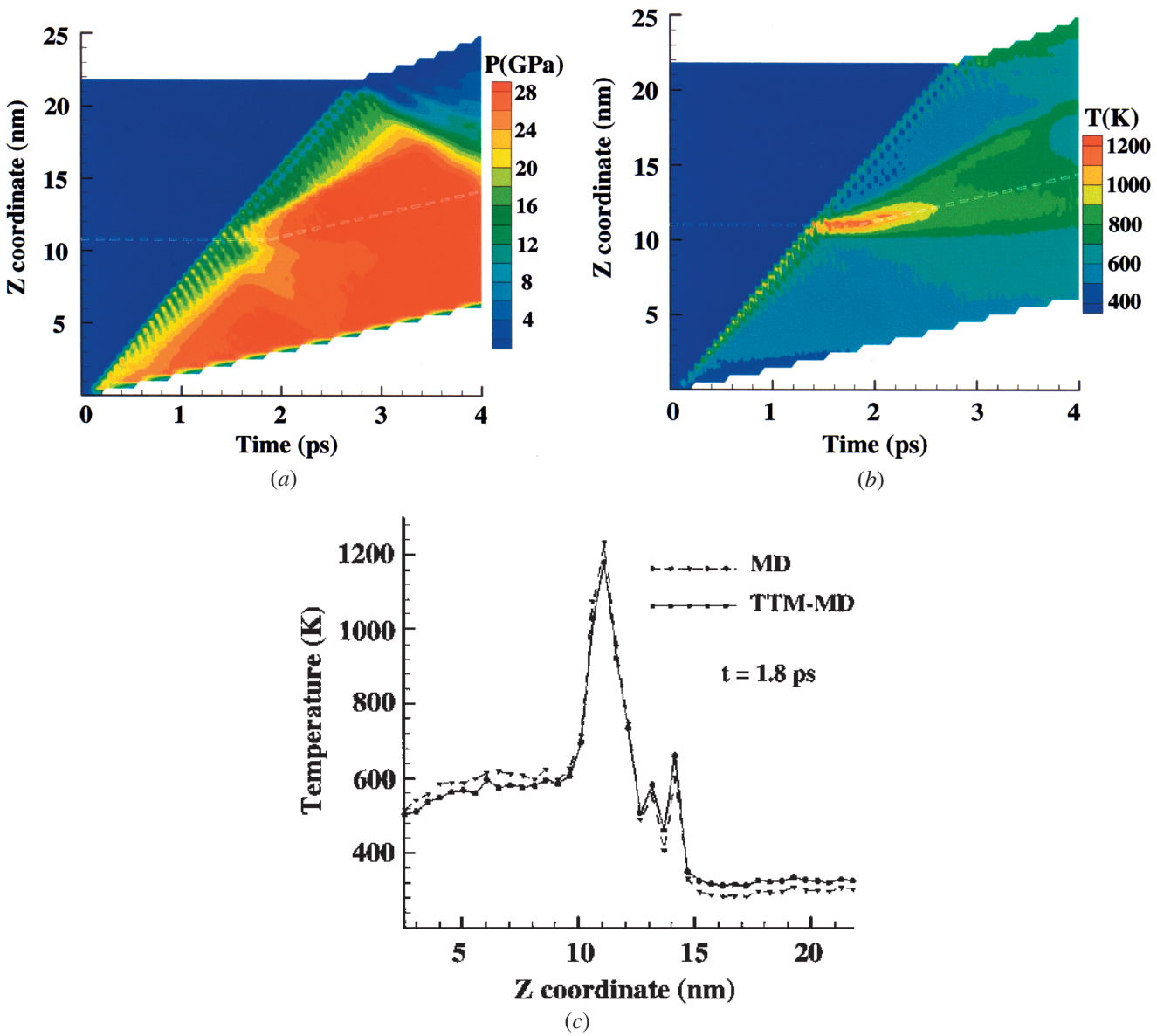

Fig. 6—(*a*) Pressure and (*b*) temperature contour plots for a TTM-MD simulation of a 300 kbar shock in an Al sample with a single, tilt GB. The magnitudes of the pressure and temperature are given by the color bars on the right of the figures, and the dashed line shows the trajectory of the shocked grain boundary. (*c*) Temperature profiles for the MD and TTM-MD simulations at $t = 1.8$ ps. [37]

used in the TTM-MD simulations for the electronic temperature are given in Reference 40.

Both the MD and TTM-MD simulations were run for 4 ps, so that the shock wave had enough time to reach the back surface but the reflected wave did not return to the GB. The temperature- and pressure-contour plots are shown in Figures 6(a) and (b), respectively, for the TTM-MD simulation. In the pressure plot (Figure 6(a)), a partial reflection of the shock ($v_{\text{shock}} \sim 7.5$ km/s) from the GB can be observed at ~1.5 ps, and a complete reflection of the shock wave from the back surface of the computational cell can be observed at ~3 ps. After the shock reaches the GB, the GB starts to move with the piston velocity, as expected. In the temperature-contour plot (Figure 6(b)), the interaction of the shock wave with the GB leads to a transient thermal spike of nearly a factor of 2 in the GB region, as shown in Figure 6(c) at a time of 1.8 ps. Later in time, the GB region remains roughly 200 K hotter than the surrounding regions. This simulation indicates that the temperature at the GB is higher than in the surrounding material, due both to its lower density and an impedance mismatch or compressibility incompatibility between the two grains. This higher temperature can induce disordering at the GB and raises the possibility that after the second, much stronger shock (160 GPa), the GB could be hot enough to melt, or lose most of its strength.

To assess the effect of possible GB softening on the RT dynamics, "mesoscale" simulations were done using the ARES computer code. For these simulations, the GB regions and grain-interior regions were explicitly zoned up and run as separate regions. Strength was turned off ($\sigma = 0$) in the GB regions, to represent liquid grain boundaries, but $\sigma = \sigma_{SG}$ (nominal Steinberg–Guinan strength) elsewhere. The results at 12 ns are shown in Figure 7(a), where the 20 μm ripple is starting to grow. The color corresponds to strength (red = strong, blue = weak, and white = liquid), so the white regions represent $\sigma = 0$ at the grain boundaries. The results at 12 ns for three separate calculations are shown in Figure 7(b), showing that growth was the largest for the $\sigma = 0$ simulation and the smallest for $\sigma = \sigma_{SG}$. As anticipated, the mesoscale simulation falls in between. Growth factors of peak-to-valley spatial amplitude *vs* time for these three simulations are shown in Figure 7(c). The upper curve corresponds to $\sigma = 0$ everywhere, the lower curve represents $\sigma = \sigma_{SG}$ everywhere, and the intermediate curve represents the case where $\sigma = \sigma_{SG}$ everywhere except at the GBs, where $\sigma_{GB} = 0$. Note that both the upper ($\sigma_{GB} = 0$) and lower ($\sigma = \sigma_{SG}$) curves in Figure 7(c) are similar to their corresponding curves in Figure 4(c), although the simulations shown in Figure 4 (LASNEX) and Figure 7 (ARES) used completely different codes and were done by different theorists. This demonstrates the ability to simulate these high-strain-rate experiments reliably, so that comparisons with the experimental data are meaningful. This mesoscale simulation shown in Figure 7(c), falls in between the all-liquid and all-solid results, and is in better agreement with the data in Figure 4(c), at least at early time. Hence, mesoscale dynamics could be a plausible explanation for the observed RT data shown in Figure 4.

In summary, there are several scenarios that could lead to the observed RT data. (1) In one scenario, there is some mechanism, such as microshear bands or melted GBs, that cause the material to flow nearly liquidlike early in time. Later in time ($t > 12$ to 13 ns), the material recovers bulk solidlike properties, but exhibits enhanced strength, consistent with $G_{SG}/10$ in the Steinberg–Guinan model. This might suggest that dislocation transport has been severely inhibited, and the material responds like an ideal crystal. For example, if the GB melted, then rapidly resolidified to an amorphous state, this might effectively "turn off" dislocation transport as the deformation mechanism. (2) If phonon drag is the dominant mechanism, not unphysically large values of D/ρ_m can be found that would give this enhanced strength. (3) Alternatively, phonon drag could be the operative mechanism throughout the entire deformation, so that $\sigma \approx D\dot{\varepsilon}/\rho_m \mathbf{b}$ both at early and late times. Again, if ρ_m or D/ρ_m is treated as a free parameter, reasonable values could be found that would allow the simulation to roughly reproduce the data. (4) Finally, the time-dependent deformation might require a mesoscopic description. For example, if the GBs are assumed to be liquid or to have otherwise failed ($\sigma_{GB} \rightarrow 0$), and grain interiors to be solid, obeying nominal Steinberg–Guinan strength, then mesoscale simulations can roughly reproduce the data. All of these scenarios allow simulations that are roughly consistent with the experiment to within the uncertainties of the data. Unfortunately, the data are too sparse and have too much scatter to differentiate between these different pictures.

V. RECOVERY OF DRIVEN SAMPLES

In this section, the implementation and use of sample recovery to infer deformation mechanisms and integral quantities about the drive and sample are discussed. In Figure 8(a), we show the results at a time of 1 μs from the 2-D hydrodynamics code CALE of the crater formation process.[41] The simulation assumed a shockless drive similar to those shown in Figure 2, with a peak pressure of 50 GPa. In this particular design, a phase plate with super-Gaussian laser spot of intensity profile given by $I = I_0 \exp[-(r/a)^{4.7}]$, with $a = 412$ μm, was used. Taking into account the angles of incidence, this generates a 90 pct–to–90 pct (in laser intensity) spot of diameter ~600 μm. This spot size is of the order the spatial scales of interest, such as the depth and diameter of the crater. Therefore, 2-D simulations of the sample, calibrated against the crater dimensions, are used to estimate the material conditions (P, ρ/ρ_0, and T) *vs* position and time in the sample. Note that an incipient spall layer appears in Figure 8(a). The sample here was thick enough that it was not accelerated off the target holder. Samples thinner than a few hundred microns are, however, accelerated by this drive. The soft-recovery apparatus captures these samples in a tube several centimeters long filled with SiO_2 aerogel, at densities ranging from 50 to 200 mg/cm^3.

We show in Figure 8(b) an experimental result of a crater in a recovered, large-grained A16061 sample driven by the shockless drive discussed previously, only with a peak pressure of 37.5 GPa. The Al sample has been sectioned and etched to show the crater shape and grain structure of the metal. The overall crater depth is about 300 μm, in agreement with simulations,[41] and there is structure evident in its shape. The details of the shape of the crater are still being analyzed. The limited data analyzed to data suggest that the maximum depth of the crater (h_{crater}) varies directly with the peak pressure of the drive[41] and can roughly be approximated as $h_{\text{crater}} \approx (9\ \mu\text{m/GPa}) P_{\max}(\text{GPa})$.

Conversely, if the drive pressure is well known, then the crater depth can serve as an integral measure of material

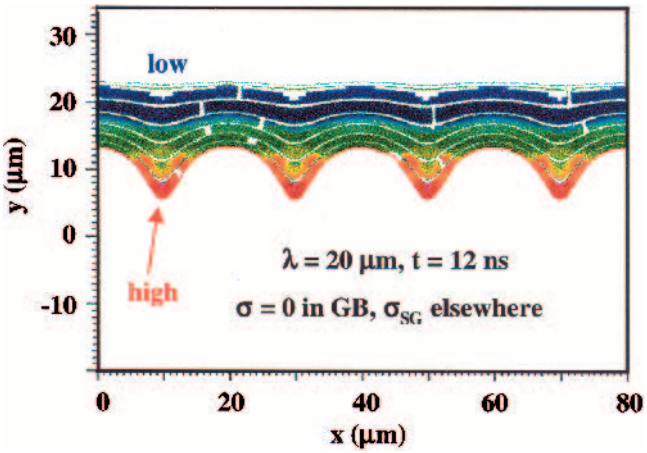

(*a*)

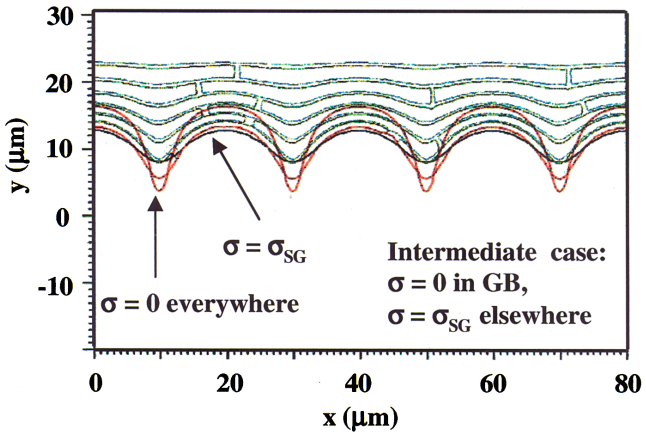

(*b*)

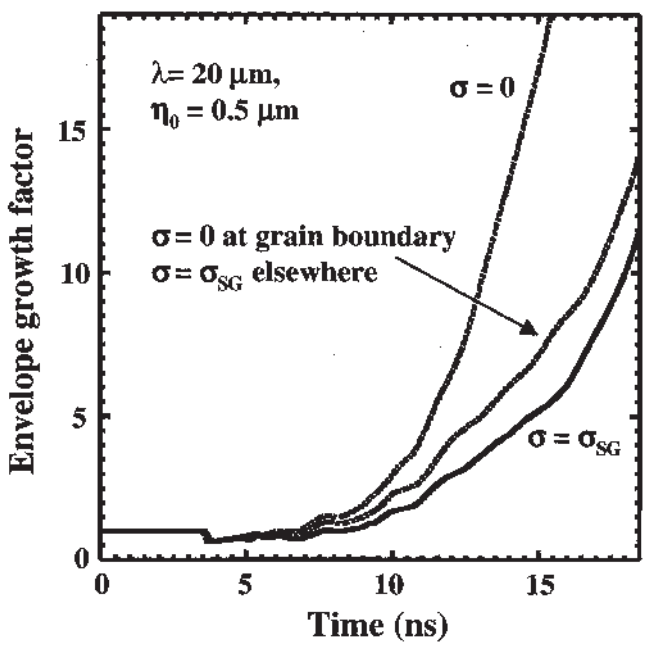

(*c*)

Fig. 7—(*a*) ARES 2-D "mesoscale" simulations, treating the grain boundary (GB) regions differently than the grain interiors. The color scale corresponds to strength (σ) with white representing $\sigma = 0$, blue being low strength, and red being the highest strength. (*b*) Similar to (a) except the interface profile is shown for three different simulations at the same time, corresponding to $\sigma = 0$ everywhere, $\sigma = \sigma_{SG}$ everywhere, and $\sigma = 0$ in the GB region but $\sigma = \sigma_{SG}$ elsewhere. (*c*) The predicted perturbation growth factors of peak-to-valley spatial amplitudes *vs* time for the ARES mesoscale simulations for the three cases described in (*b*). The experimental resolution was not accounted for in these simulation results.

strength. This is illustrated in Figure 8(c), where crater depth *vs* material strength is plotted from 2-D simulations, assuming a peak pressure of ~14 GPa. If, for example, the strength of the sample is changed by a factor of 2, the crater depth is predicted to change by about 50 pct, which should be readily apparent. Also, if regions of the sample melted then resolidified, this should be apparent in the grain-size distribution, allowing a residual melt depth to be inferred. We see no indication in Figure 8(b) of melt-refreeze activity.

To illustrate the use of recovery to infer a deformation mechanism, we show in Figure 9 the results of recovered samples from shock-compressed single-crystal Cu.[35,36,42,43] Samples of ~1-mm-thick single-crystal Cu were shock compressed along the [001] direction by laser illumination with 40 to 320 J of laser energy in a 3.5-ns pulse in a 2.5-mm-diameter spot on the Omega laser. Since the laser spot size was considerably larger than the sample size, these samples experienced a roughly 1-D shock compression. Hence, 1-D simulations matched against separate shots measuring shock breakout times[43] are used to infer the (P, ρ/ρ_0, and T) conditions of the sample *vs* (z, and t). Since the laser pulse duration is short, the strength of the shock wave that is generated decays as it moves through the sample. For example, for the 320 J laser shot, the shock decays from ~100 GPa at the front surface to ~10 GPa at 1 mm into the sample. The samples were recovered from a foam-filled recovery tube, sectioned, and analyzed by transmission electron microscopy (TEM).

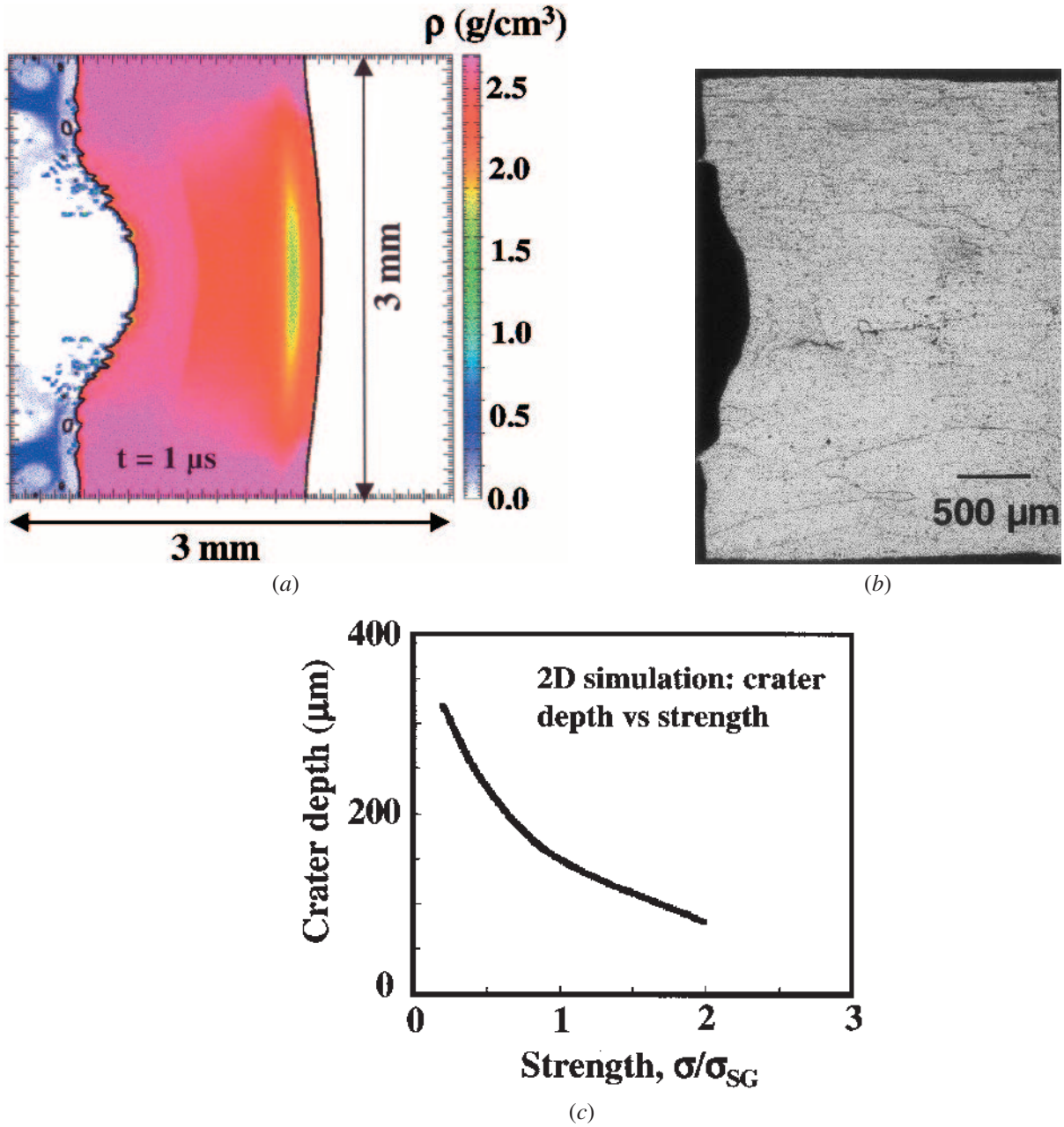

Fig. 8—CALE (2-D) simulation of crater formation in thick A16061-T6, shown at 1 μs. (*b*) Experimental crater image in thick A16061 for a drive similar to that shown in Fig. 2 only with peak pressure of 37.5 GPa. (*c*) Prediction from the 2-D simulations of the sensitivity of crater depth *vs* material strength.[41]

The image shown in Figure 9(a) shows the residual microstructure resulting from an ~12 GPa shock, and the image in Figure 9(b) corresponds to an ~40 GPa shock. These pressures correspond to the maximum shock strengths at a distance of 50 μm into the sample on the laser-illumination side, for laser energies of 40 and 205 J, respectively. There is a very distinct difference in the residual microstructures. The dislocation cell structure shown in Figure 9(a) corresponds to the residual tangled dislocations that result from shock deformation due to slip along the 12 dominant slip systems: four {111} slip planes and three <110> glide directions within each of these planes. It is generally assumed that the shock front generates a homogeneous distribution of dislocations to accommodate the shock deformation. After shock passage, the dislocations organize or migrate into this cell structure, corresponding to dense dislocation tangles in cell walls and cell interiors of diameter d_{cell} = 0.3 to 0.6 μm exhibiting a significantly lower residual dislocation density. This postshock migration is driven by the attractive and repulsive forces between dislocations, that is, the so-called Peach–Kohler force. An order-of-magnitude estimate can be made of the time interval to form this residual dislocation cell structure. Assume that the cells are formed on a characteristic time scale set by the ratio of cell size and characteristic dislocation velocity and assume that dislocations move at 20 pct of the shear-wave velocity. Then, $t_{cell} \sim d_{cell}/(v_{disloc}) \sim d_{cell}/(0.2c_{shear}) \sim (4\ \mu m)/(0.2(G/\rho)^{1/2}) \sim (4\ \mu m)/(0.5\ \mu m/ns) \sim 8$ ns. This suggests that these cells should form on a ~10 ns time scale after shock passage.

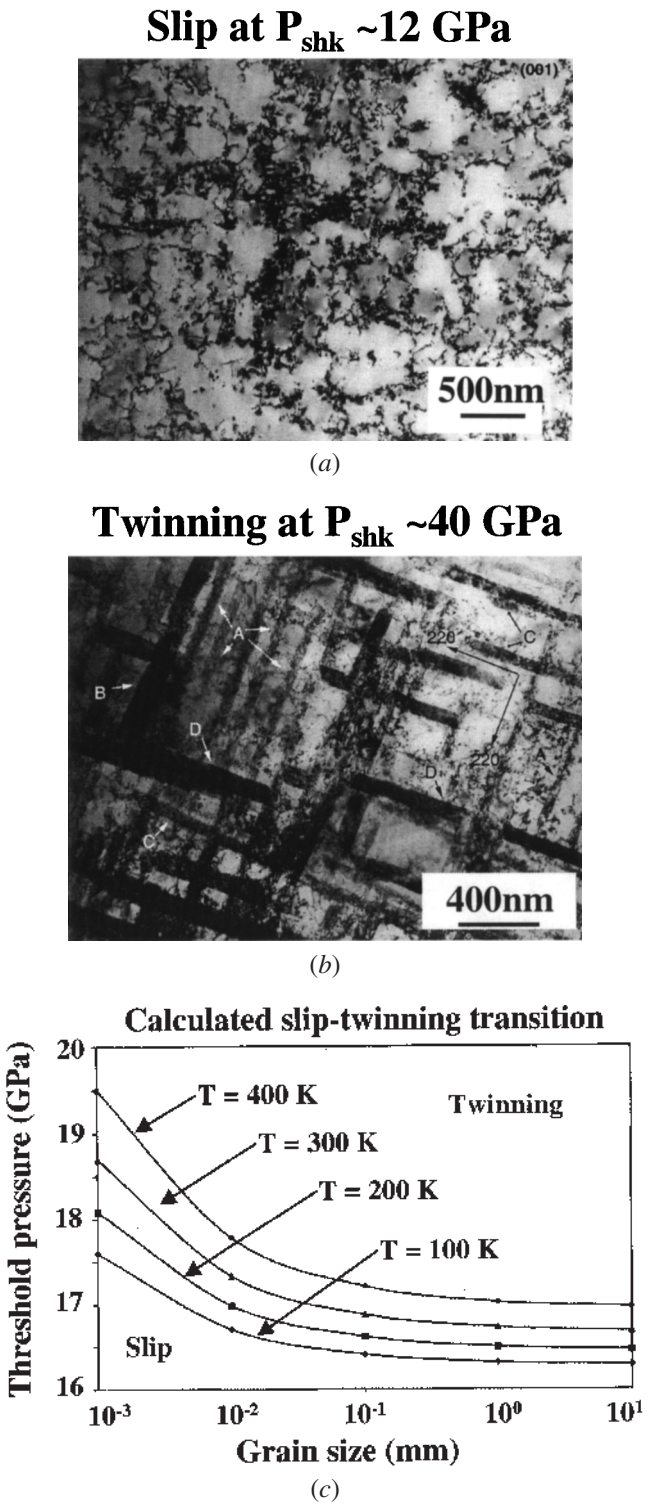

Fig. 9—(*a*) TEM characterized single-crystal Cu sample shocked (P_{shock}~12 GPa) at the Omega laser. (*b*) Same, only for a stronger shock (P_{shock}~40 GPa). (*c*) Theoretical slip-twinning threshold prediction.[35,36]

The residual microstructure shown in Figure 9(b) is considerably different from that shown in Figure 9(a). This image is the result of a TEM analysis with an electron-beam direction of $B = <001>$, and the (electron) diffraction plane corresponds to (200). The distinct cross-hatched pattern represents traces of {111} planes on (001), that is, the edge-on view of the four {111} planes cutting the (001) plane. The different hues in the crisscross pattern represent stacking-fault bundles or regions of microtwins. All four stacking-fault variants, $(111)\frac{1}{6}[\bar{1}\bar{1}2]$, $(11\bar{1})\frac{1}{6}[112]$, $(\bar{1}11)\frac{1}{6}[1\bar{1}2]$, and $(1\bar{1}1)\frac{1}{6}[1\bar{1}2]$, are observed (that is, a displacement of $\frac{1}{6}[\bar{1}\bar{1}2]$ due to a residual partial dislocation, along the (111) slip plane, and so on) and are indicated by A, B, C, and D, respectively, in the figure. Given that the laser-induced shock direction was <001>, all four {111} primary slip planes should be activated with equal probability, having the same Schmid factor of 0.4082.[35]

Similar results, both for dislocation cells and for twinning, have been observed by Murr using shocks launched with a HE drive.[44] The "dwell time" for these shocks (the time interval over which pressure is maintained behind the shock) is of the order of ~1 μs, whereas for the laser-induced shock, the dwell time is of the order of 10 ns, that is, a factor-of-100 shorter. This suggests that the observed residual microstructures shown in Figures 9(a) and (b) were formed promptly at the shock front. Hence, the same prompt material response at the shock front can be studied on laser-driven systems, where time-resolved diagnostics can be implemented to diagnose the dynamics as it happens, with subnanosecond time resolution.

The comparison between the residual dislocation cells shown in Figure 9(a) and the microtwins shown in Figure 9(b) is interesting, because it suggests a twinning shock threshold between 12 and 40 GPa. This threshold can be estimated analytically, as shown in Figure 9(c), by assuming that slip and twinning are competing processes.[35,36] Empirically, it is known that twinning is rather insensitive to temperature and strain rate, whereas slip is not. Therefore, it is expected that at low strain rates (weak shocks), slip should be the dominant mechanism for deformation, whereas at high strain rates (strong shocks), twinning should dominate. Conversely, at low temperatures, twinning should dominate, whereas at higher temperatures, slip should take over. The analytic estimate[35,36] for Cu assumes that the stress required for twinning is independent of strain rate and temperature. The transition shock strength from slip to twinning is then found by equating the flow stresses for each, $\sigma_{twinning} = \sigma_{slip}$. The flow stress for slip is taken from the MTS model,[12,18] modified to include a Hall–Petch term and a work-hardening factor. The strain rate at the shock front is estimated by the empirical Swegle–Grady relation, $\dot{\varepsilon} \sim P_{shk}^4$.[45] The results lead to an estimate of the critical shock pressure above which twinning dominates and below which slip is the preferred deformation mechanism. This is shown for different initial temperatures and grain sizes in Figure 9(c). For room-temperature ambient conditions and single-crystal samples, this estimate gives $P_{twinning} = 16$ to 17 GPa, which is consistent with the observations shown in Figures 9(a) and (b).

VI. LATTICE RESPONSE

We now discuss two time-resolved microscale diagnostics developed to probe the microscopic lattice response, dynamic diffraction, and EXAFS measurements. These two diagnostics offer the potential to infer such fundamental quantities as the phase, Peierls barrier, dislocation density, and lattice temperature. Experiments done with single crystals are well suited to the time-resolved diffraction diagnostic. If a shock or compression wave traverses a single crystal, the lattice

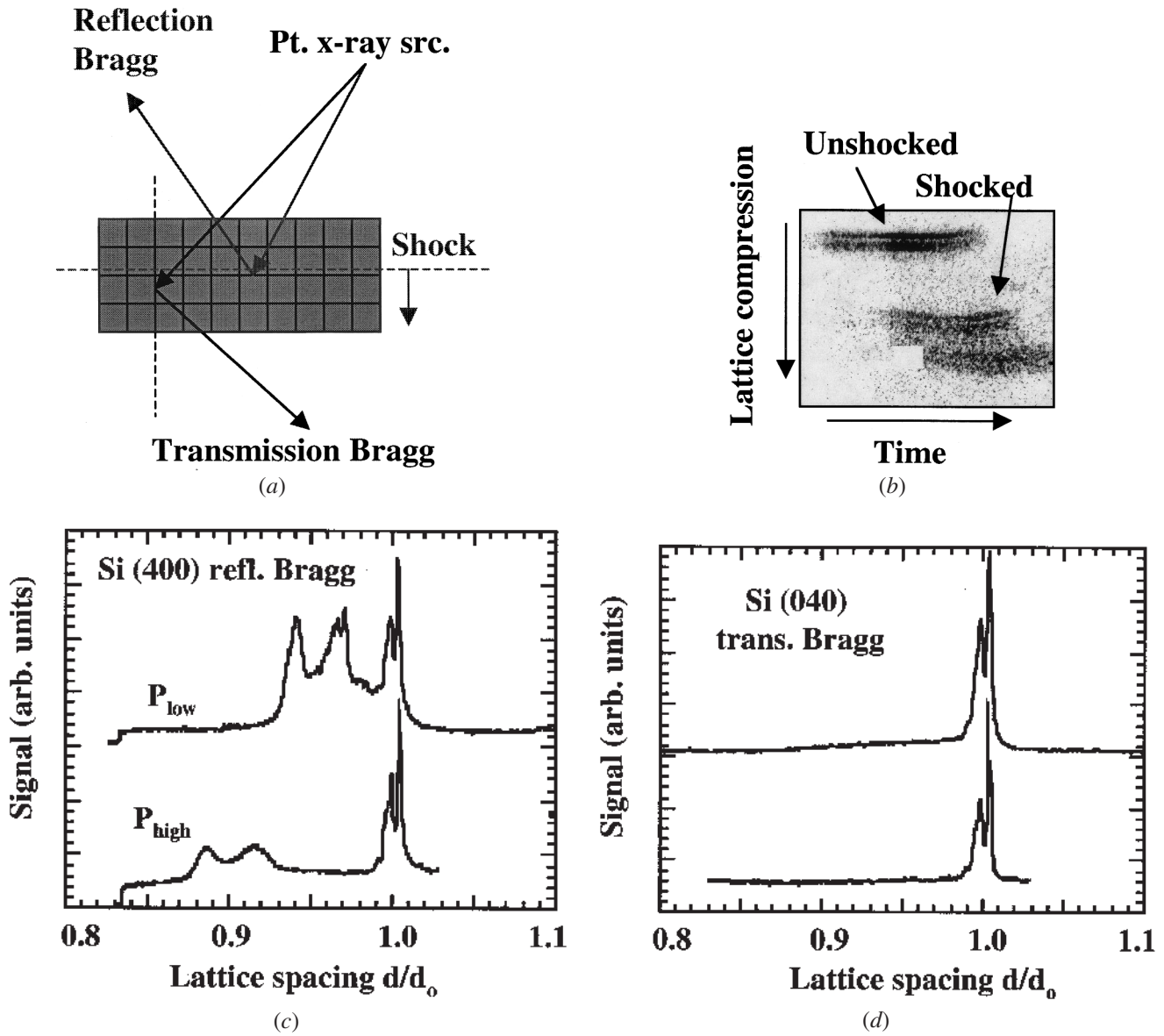

Fig. 10—(*a*) Initial configuration for Bragg diffraction experiments. (*b*) Raw streaked data for Bragg diffraction off shocked Si crystal. (*c*) Time integrated result for reflection Bragg diffraction for shocked Si. (*d*) Same only for transmission Bragg diffraction. (*e*) and (*f*) Same, only for Cu.[47]

planes compress. This can be observed by recording a Bragg diffraction signal, both in reflection and in transmission, as illustrated in Figure 10(a). If a shock is launched from the top to bottom in Figure 10(a) through, say, a 40-μm-thick single-crystal Si sample, the shock compression can be tracked by streaking the diffraction signal (aligning the diffraction image onto the slit of an X-ray streak camera), as shown by the raw image in Figure 10(b).[46,47] Initially, there is diffraction only from the unshocked region. Later in time, there are regions of the Si that have been shocked and regions that remain unshocked. If the X-ray probe is of high-enough energy (~5 keV here), both shocked and unshocked regions can be observed simultaneously, as shown in the streaked image. A time-integrated image can also be recorded onto X-ray film, profiles from which are shown in Figures 10(c) through (f) Figures 10(c) and (d) correspond to 40-μm-thick single-crystal Si and the geometry indicated in Figure 10(a). This experiment was done on the Nova laser using a hohlraum drive, similar to that shown in Figure 3. Figures 10(e) and (f) correspond to a similar experiment done on the Omega laser, using a 2-μm-thick single-crystal Cu sample shocked in the [001] direction by direct laser illumination.[46,47] Both Si and Cu show lattice compression in the reflection Bragg data. The transmission Bragg detector, however, was oriented to diffract off lattice planes orthogonal to the direction of shock propagation, thus measuring transverse lattice compression (Figure 10(a)). For the shocked Si crystal, there was no observed transverse compression, to within the limits of sensitivity of the diagnostic, whereas for the Cu sample, there was prompt relaxation to a symmetric three-dimensional (3-D) compression (quasihydrostatic). It appears that the Si crystal was compressed uniaxially over the 5-ns duration of the shock experiment, whereas the Cu crystal was compressed nearly hydrostatically. One interpretation of this process is as follows. Relaxation to a 3-D compression requires dislocation movement, as described

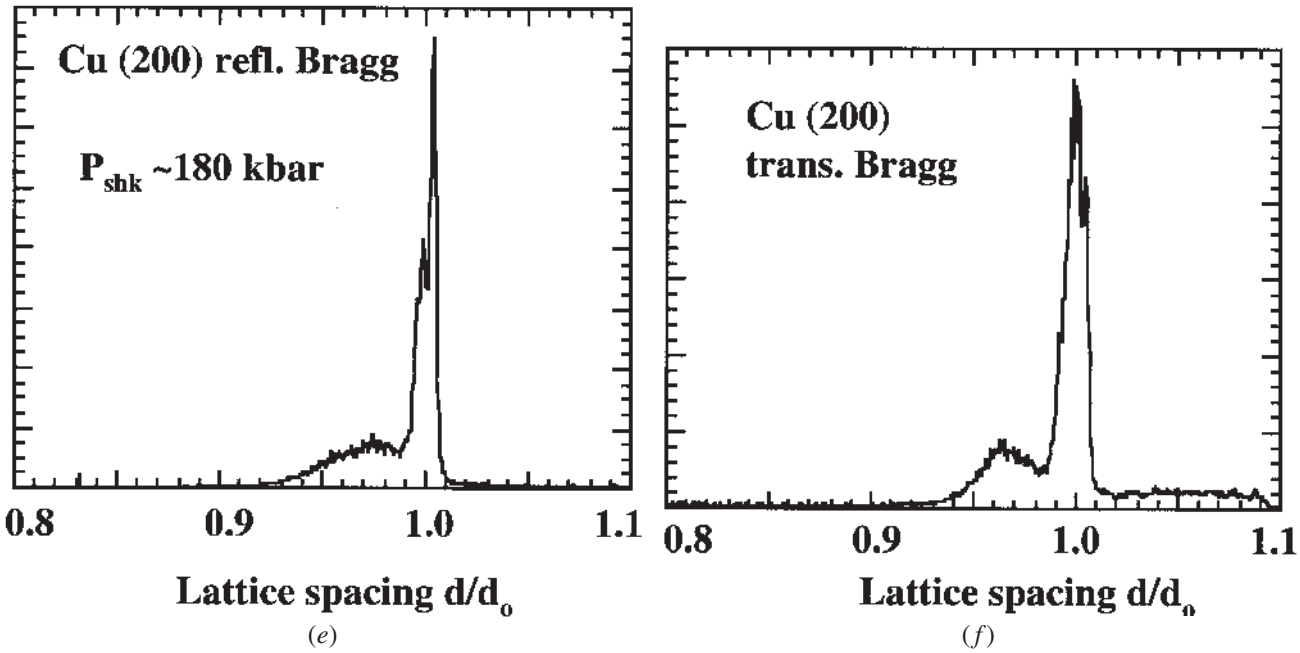

Fig. 10 (continued.)—(*a*) Initial configuration for Bragg diffraction experiments. (*b*) Raw streaked data for Bragg diffraction off shocked Si crystal. (*c*) Time integrated result for reflection Bragg diffraction for shocked Si. (*d*) Same only for transmission Bragg diffraction. (*e*) and (*f*) Same, only for Cu.[47]

by Orowan's equation, $\dot{\varepsilon} = \rho_m \mathbf{b} \bar{v}_d$ (Section II). The factors determining $d\varepsilon/dt$ are the mobile dislocation density and the average dislocation speed. But, $<v_d>$ is a function of the Peierls barrier. At a given T value, if σ_P is high, $<v_d>$ and, hence, $d\varepsilon/dt$ are low, because the mobile dislocations stay pinned for long intervals of time. Materials with a low mobile dislocation density or high Peierls barrier (stress), will have a low $d\varepsilon/dt$ value, and the transition to 3-D compression will take longer. The Peierls barrier in fcc metals such as Cu is very low ($\sigma_P \sim (10^{-6}$ to $10^{-5})G$) where here G is the shear modulus.[4] Covalent crystals such as Si, on the other hand, have a large barrier, $\sigma_P \sim (10^{-2})G$. Furthermore, silicon has a very low ρ_m value. Hence, the time to transition to 3-D compression for Si will be very long compared to Cu, qualitatively explaining the observed difference in behavior between Si and Cu illustrated in Figure 10. These data and analysis show the potential value of time-resolved diffraction for microscopically probing lattice response to infer bounds on Peierls stress and mobile dislocation density in dynamically deforming crystals. It has also been pointed out that comparing the different compressions of orthogonal lattice planes with multiple lattice-plane diffraction offers a microscopic measure of lattice strength.[36]

Whereas diffraction probes the long-range order of a lattice, EXAFS measurements probe the lattice short-range order. The basis for this diagnostic is illustrated in Figure 11(a).[48,49,50] When an atom absorbs an ionizing, high-energy X-ray, an electron rises from a bound state into the continuum. The outgoing wave packet of the free electron, illustrated by the concentric solid circles in Figure 11(a), scatters off of neighboring atoms, as illustrated by the dashed circular curves. The outgoing and reflected waves interfere with each other. The square of the total electron wave function is what determines the probability of the process, and this interference is, therefore, observed in fine structure in the X-ray absorption just above an opacity edge. The X-ray absorption probability for a photon of energy (E_γ) can be written as (1 − f), where $f = I/I_0 = e^{-\rho\kappa x} = e^{-\mu x}$. Here κ (cm^2/g) is the opacity, μ (cm^{-1}) is the energy-dependent absorption coefficient, I_0 corresponds to a flux of X-rays (photons/cm^2 s) incident on a sample of thickness x and density ρ, and I corresponds to the transmitted flux. The absorption coefficient ($\mu(E_\gamma)$) is energy dependent. Since the electron-wave number (k) after absorbing the X-ray corresponds to $\hbar^2k^2/2m_e = E_\gamma - E_{\text{edge}}$, then $\mu(E_\gamma) = \mu(k)$ is also a function of k. The normalized absorption probability can then be written as

$$\chi(k) = \frac{\mu(k) - \mu_0(k)}{\mu_0(k)} \qquad [9a]$$

where $\mu_0(k)$ represents the smooth absorption above the edge corresponding to an isolated atom (no interference modulations). For K-edge absorption, the standard EXAFS equation can be written as[48,51–53]

$$\chi(k) = \sum_j \frac{N_j}{kR_j^2} F_j(k) \sin(2kR_j + \phi_j(k)) e^{-2\sigma_j^2 k^2} e^{-2R_j/\lambda(k)} \qquad [9b]$$

The summation is over coordination shells, N_j is the number of atoms in the shell, and R_j is its radius. The $F_j(k)$ factor corresponds to the backscattering amplitude for the electron-wave function reflected from the jth coordination shell. The $\phi_j(k)$ term represents a phase shift due to the electron-wave packet moving through a varying potential. The exponential, $e^{-2\sigma_j^2 k^2}$, represents the Debye–Waller factor, which reduces the coherent interference of the EXAFS signal due to thermal fluctuations in the local scattering atoms. The $e^{-2R_j/\lambda(k)}$ factor represents the attenuation of the electron-wave function due to the finite mean free path ($\lambda(k)$) of the ejected electron.

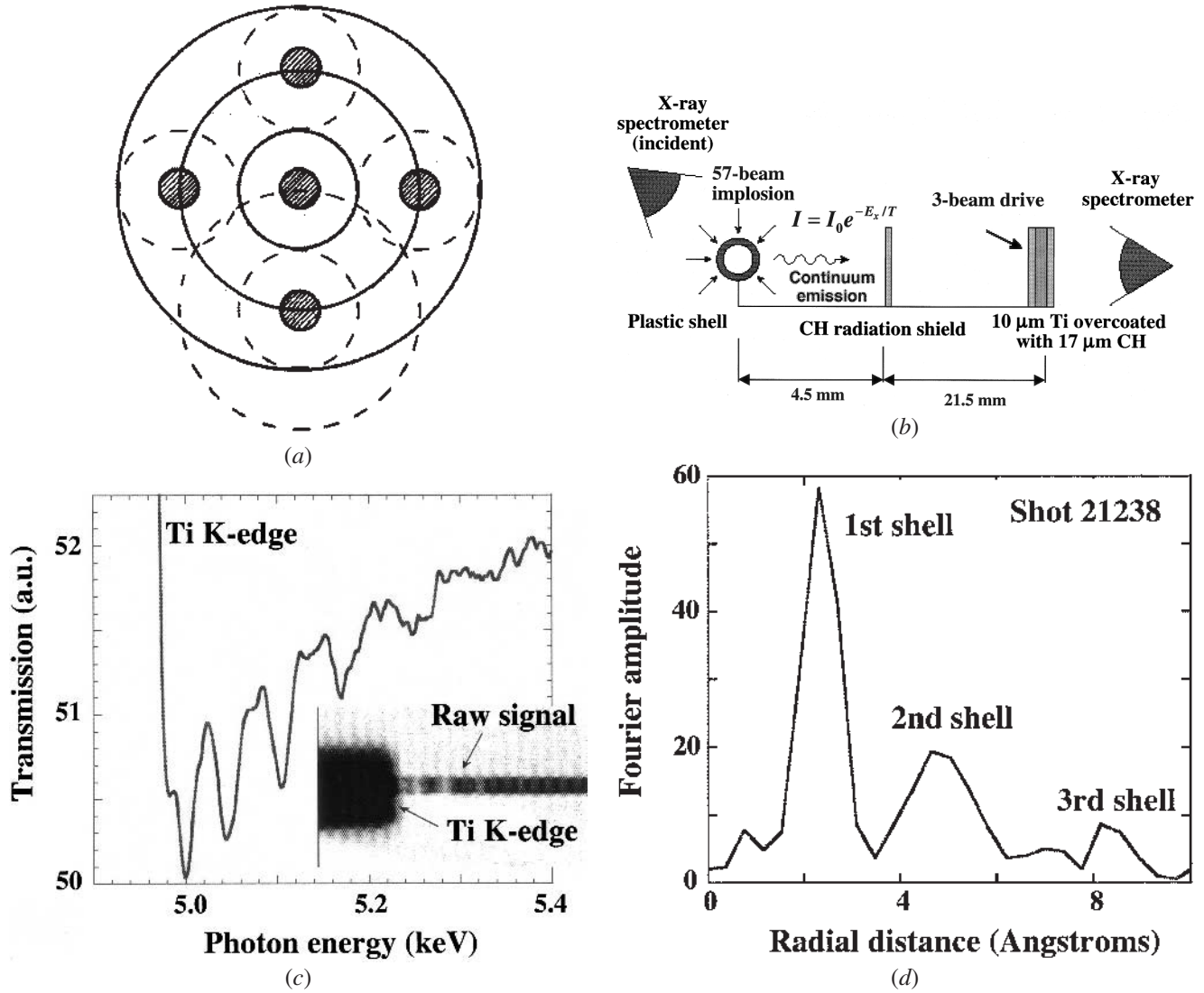

Fig. 11—(*a*) Schematic for the electron wave packet interference that underlies the EXAFS diagnostic technique.[48] (*b*) Experimental configuration for the EXAFS measurements at the Omega laser. (*c*) Raw EXAFS absorption spectrum for unshocked, room-temperature Ti. (*d*) The inferred electron radial distribution function for the data shown in (*c*).[51]

We have recently developed a time-resolved EXAFS diagnostic with the Omega laser.[51–53] The experimental setup is shown in Figure 11(b). Three 1-ns-square laser beams, stacked back to back to make a 3-ns-square drive pulse, are used to shock compress a 10-μm-thick sample of Ti embedded in 17-μm-thick CH on either side, and the remaining 57 beams implode an inertial confinement fusion capsule. This implosion generates a short ($\sim$100 ps) burst of spectrally smooth hard X-rays, $I = I_0 \exp(-E_\gamma/T)$, to be used for the EXAFS absorption. Typical values for the implosion X-ray spectrum are $I_0 = 2$ to 3×10^{19} keV/keV and temperature $T = 1.25$ keV. A measured raw EXAFS absorption spectrum showing the modulations just above the *K*-edge for room-temperature Ti is shown in Figure 11(c). A typical Fourier analysis transforms $k\chi(k)$ to give the electron radial distribution function,[48,51] as shown in Figure 11(d), where the first three coordination shells are evident.

The simplest analysis selects only the first coordination shell from Figure 11(d), ignoring the effects of multiple scattering, and converts back to *k*-space, as shown in Figure 12(a), where $k\chi = k(\mu - \mu_0)/\mu_0$ is plotted.[51–53] This is the form of the data that is fitted with Eq. [9b], as shown in Figure 12(a). Fits of the measurements with EXAFS theory (Eq. 9) give an accurate determination of the density (compression) to better than $\sim$4 pct through the period of modulation. In addition, the temperature is determined from the damping rate through the Debye–Waller factor, as shown in Figure 12(b). Note that the modulations at a higher electron-wave number die out more quickly at the higher temperatures. This is because the higher wave numbers (shorter electron wave lengths) are more sensitive to the incoherence caused by the thermal fluctations of the positions of the coordination shells. It is expected that temperature can be determined to better than $\sim$25 pct by this technique. In Figure 12(c), the temperature thus determined for three different laser shots is shown, along with the results of simulations, as a function of the thickness of the CH preheat shield and sample distance from the

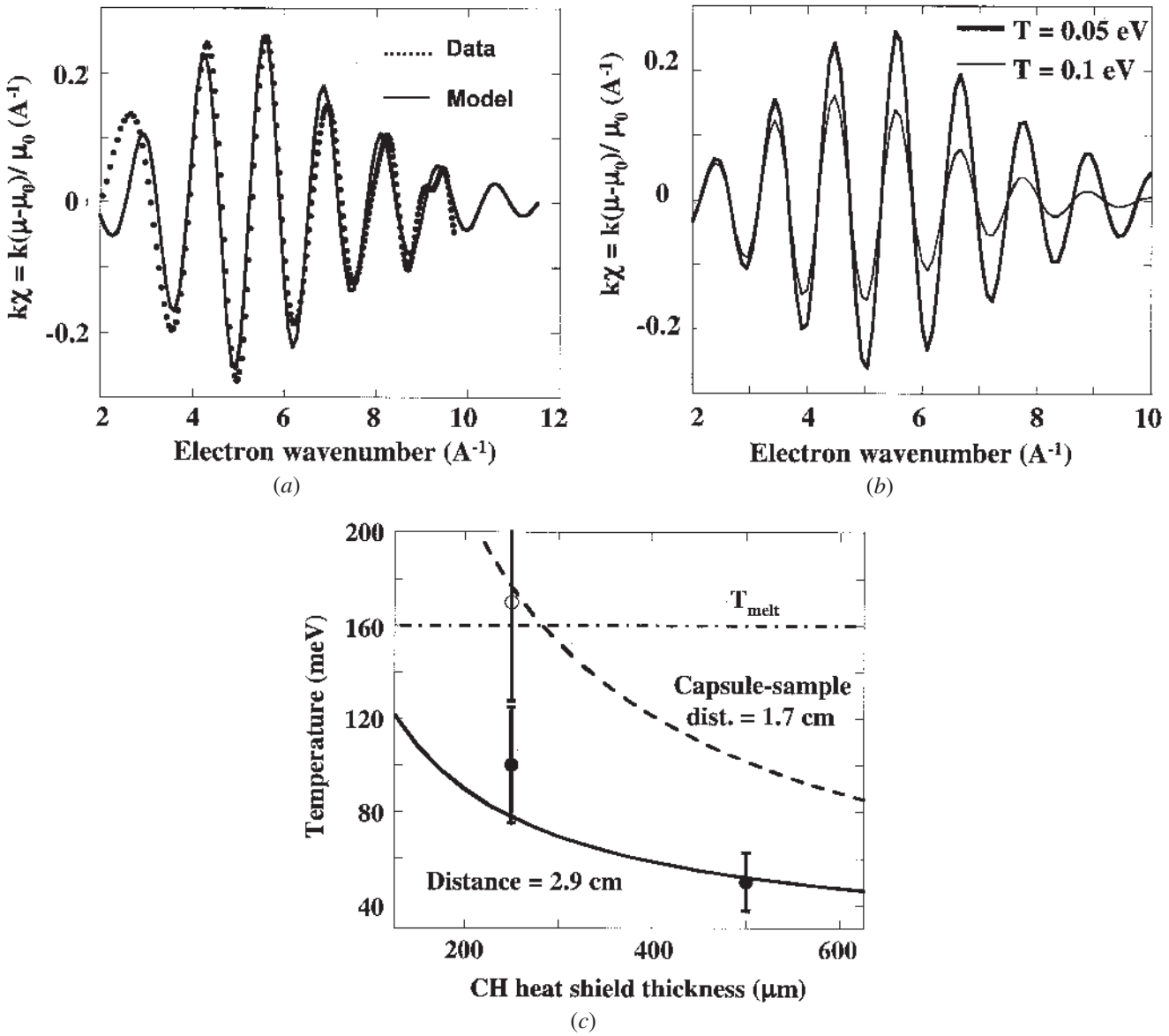

Fig. 12—(*a*) Results from the EXAFS analysis, fitting the model (Equation 9) to the data from Fig. 11, showing the quality of the theoretical fit. (*b*) Comparison of theoretical EXAFS signals for two temperatures, $T = 0.05$ eV (upper) and $T = 0.1$ eV (lower). (*c*) Temperature analysis from EXAFS measurements of Ti samples under three different temperature conditions at nominally ambient density (unshocked). The temperature is modified by varying the thickness of the CH preheat shield, shown in Fig. 11(*b*), and the distance from the backlighter (implosion) to the sample. The curves correspond to 1-D radiation-hydrodynamics simulations.[51–53] The horizontal dot-dashed line corresponds to the melt temperature of Ti at ambient conditions.

implosion. The thinner the CH preheat shield or the smaller the distance between the backlighter implosion and sample, the higher the expected Ti temperature, as observed and simulated. The EXAFS measurement as a temperature diagnostic is sensitive down to nearly room temperature, which is important for materials-science experiments, with a time resolution of ~0.1 ns. The temperature of the sample can be modified by varying the thickness of the CH preheat shield or the distance of the sample from the backlighter implosion. As suggested by the horizontal dot-dashed line in Figure. 12(c), EXAFS should also work for temperatures up to and exceeding the melt temperature,[51] a capability that has been demonstrated in static experiments.[54]

VII. EXPERIMENTS PLANNED FOR THE NIF LASER

Up until now, we have described experiments that have been done on existing laser facilities. Pressures and strain rates achieved correspond to 10 to 200 GPa and 10^6 to 10^8 s^{-1}. With the commissioning of the new NIF laser at Lawrence Livermore National Laboratory,[25,26] an opportunity presents itself to increase the pressures of the samples in the solid state to much higher values, $P > 10^3$ GPa. It will be particularly interesting to see, for example, how the Peierls barrier, shear modulus, and material strength scale as pressure and strain rate are increased 100-fold above 10 GPa and 10^5 s^{-1}. At the other extreme for laser experiments, sample sizes approaching

~1 cm in transverse dimension and ~1 mm in thickness at pressures of a few times 100 GPa may be possible, using much larger laser spots and much longer (~100 ns) pulse lengths.

Pressure scaling should allow details about the Peierls barrier to be probed. Strain-rate scaling will be a good method for probing deformation mechanisms. Velocity-interferometer measurements allow the time-dependent drive (applied pressure *vs* time) on the sample to be well characterized spatially and temporally. Timed-resolved radiography, used in RT experiments, will allow high-pressure strength to be measured, and sample recovery should allow deformation mechanisms to be inferred. Time-resolved diffraction probes long-range lattice response to compression, allowing the strain rate and phase to be directly measured. Diffraction is also sensitive to Peierls stress, through the time scale for the 1-D–to–3-D compression transition, and may allow a lattice-level measure of strength, by the degree to which the lattice deviates from hydrostatic conditions. The EXAFS measurements probe short-range lattice response and offer a good measure of temperature in the ~100 meV range, relevant to this high-pressure materials-science work. Both diffraction and EXAFS measurements allow phase to be determined on a subnanosecond time scale. At the ultrahigh pressures ($P \gg 100$ GPa) and strain rates ($\dot{\varepsilon} \gg 10^5\ s^{-1}$) accessible, models, codes, and mechanisms can be tested in their "asymptotic limits." Initial conditions may become less important, or negligible all together, as the material responds to the extreme deviatoric stresses, pressures, and strain rates. Finally, the short time scales and small spatial scales may make it possible to calculate directly the experimental conditions with large-scale MD simulations as well as with continuum and mesoscale simulations. This will offer a rigorous test of constitutive models and interatomic potentials at the very highest strain rates and pressures, with experiments, continuum-code simulations, and MD simulations all being compared on equal footing.

ACKNOWLEDGMENTS

We are pleased to thank M. deKoning and W. Cai for providing the initial grain boundary for the MD simulations; and V. Raevsky and his group for providing details of their heterogeneous plastic flow model (under Agreement No. B512964). This work was performed under the auspices of the United States Department of Energy by the Lawrence Livermore National Laboratory under Contract No. W-7405-ENG-48.

REFERENCES

1. J.E. Dorn and S. Rajnak: *Trans. TMS-AIME*, 1964, vol. 230, p. 1052.
2. P. Guyot and J.E. Dorn: *Can. J. Phys.*, 1967, vol. 45, p. 983.
3. U.F. Kocks, A.S. Argon, and M.F. Ashby: *Thermodynamics and Kinetics of Slip*, Pergamon Press, New York, NY, 1975.
4. D. Hull and D.J. Bacon: *Introduction to Dislocations*, 3rd ed., Butterworth-Heinemann, Boston, MA, 1984.
5. John P. Hirth and Jens Lothe: *Theory of Dislocations*, 2nd ed., Krieger Publishing Co., Malabar, FL, 1982.
6. Marc A. Meyers and Lawrence E. Murr: *Shock Waves and High-Strain-Rate Phenomena in Metals: Concepts and Applications*, Plenum Press, New York, NY, 1981.
7. Marc A. Meyers: *Dynamic Behavior of Materials*, John Wiley & Sons, Inc., New York, NY, 1994.
8. Harold J. Frost and Michael F. Ashby: *Deformation-Mechanism Maps, The Plasticity and Creep of Metals and Ceramics*, Pergamon Press, New York, NY, 1982.
9. G.R. Johnson, J.M. Hoegfeldt, U.S. Lindholm, and A. Nagy: *ASME J. Eng. Mater. Technol.*, 1983b, vol. 105, p. 42.
10. F.J. Zerilli and R.W. Armstrong: *J. Appl. Phys.*, 1987, vol. 61, p. 1816.
11. F.J. Zerilli and R.W. Armstrong: *J. Appl. Phys.*, 1990, vol. 68, p. 915.
12. P.S. Follansbee and U.F. Kocks: *Acta Metall.*, 1988, vol. 36, p. 81.
13. K.G. Hoge and A.K. Mukherjee: *J. Mater. Sci.*, 1977, vol. 12, p. 1666.
14. G. Regazzoni, U.F. Kocks, and P.S. Follansbee: *Acta Metall.*, 1987, vol. 35, p. 2865.
15. D.J. Steinberg and C.M. Lund: *J. Appl. Phys*, 1989, vol. 65, p. 1528.
16. D.J. Steinberg, S.G. Cochran, and M.W. Guinan: *J. Appl. Phys*, 1980, vol. 51, p. 1498.
17. W.G. Wolfer: LLNL Internal Report No. UCRL-ID-136221, Nov. 1999.
18. S.R. Chen and G.T. Gray: *Metall. Mater. Trans. A*, 1996, vol. 27A, pp. 2994-3006.
19. D.L. Preston, D.L. Tonks, and D.C. Wallace: *J. Appl. Phys.*, 2003, vol. 93, p. 211.
20. J. Edwards, K.T. Lorenz, B.A. Remington, S. Pollaine, J. Colvin, D. Braun, B.F. Lasinski, D. Reisman, J. McNaney, J.A. Greenough, R. Wallace, H. Louis, and D. Kalantar: 2003, *Phys. Rev. Lett.*, 2004, in press.
21. T.H. Boehly, R.S. Craxton, T.H. Hinterman, J.H. Kelly, T.J. Kessler, S.A. Kumpan, S.A. Letzring, R.L. McCrory, S.F.B. Morse, W. Seka, S. Skupsky, J.M. Soures, and C.P. Verdon: *Rev. Sci. Instrum.*, 1995, vol. 66, p. 508.
22. J.F. Barnes, P.J. Blewett, R.G. McQueen, K.A. Meyer, and D. Venable: *J. Appl. Phys.*, 1974, vol. 45, p. 727; J.F. Barnes, D.H. Janney, R.K. London, K.A. Meyer, and D.H. Sharp: *J. Appl. Phys.*, 1980, vol. 51, p. 4678.
23. P.M. Celliers, G.W. Collins, L.B. Da Silva, D.M. Gold, and R. Cauble: *Appl. Phys. Lett.*, 1998, vol. 73, p. 1320.
24. Dennis Hayes, John Vorthman, and Joe Fritz: LANL Internal Report No. LA-13830-MS, May 2001.
25. J.A. Paisner, E.M. Campbell, and W.J. Hogan: *Fusion Technol.*, 1994, vol. 26, p. 755.
26. W.J. Hogan, E.I. Moses, B.E. Warner, M.S. Sorem, and J.M. Soures: *Nucl. Fusion*, 2001, vol. 41, p. 567.
27. K.T. Lorenz: LLNL, L-021, Livermore, CA, private communication, 2003.
28. D.H. Kalantar, B.A. Remington, E.A. Chandler, J.D. Colvin, D. Gold, K. Mikaelian, S.V. Weber, L.G. Wiley, J.S. Wark, A.A. Hauer, and M.A. Meyers: *J. Impact Eng.*, 1999, vol. 23, p. 409.
29. D.H. Kalantar, B.A. Remington, J.D. Colvin, K.O. Mikaelian, S.V. Weber, L.G. Wiley, J.S. Wark, A. Loveridge, A.M. Allen, A. Hauer, and M.A. Meyers: *Phys. Plasmas*, 2000, vol. 7, p. 1999.
30. J. Colvin, M. Legrand, B.A. Remington, G. Schurtz, and S.V. Weber: *J. Appl. Phys.*, 2003, vol. 93, p. 5287.
31. K. Mikaelian: *Phys. Rev. E*, 1996, vol. 54, p. 3676.
32. K.S. Budil, T.S. Perry, S.A. Alvarez, D. Hargrove, J.R. Mazuch, A. Nikitin, and P.M. Bell: *Rev. Sci. Instrum.*, 1997, vol. 68, p. 796.
33. J. Lipkin and J.R. Asay: *J. Appl. Phys.*, 1977, vol. 48, p. 182.
34. A. Kumar, F.E. Hauser, and J.E. Dorn: *Acta Metall.*, 1968, vol. 16, p. 1189.
35. M.S. Schneider, B.K. Kad, F. Gregori, D. Kalantar, B.A. Remington, and M.A. Meyers: *Metall. Mater. Trans. A*, 2004, vol. 35A, pp. 2633-46.
36. M.A. Meyers, F. Gregori, B.K. Kad, M.S. Schneider, D.H. Kalantar, B.A. Remington, G. Ravichandran, T. Boehly, and J.S. Wark: *Acta Mater.*, 2003, vol. 51, p. 1211.
37. Dmitriy S. Ivanov, Leonid V. Zhigilei, Eduardo M. Bringa, Maurice De Konig, Bruce A. Remington, Maria Jose Caturla, and Stephen M. Pollaine: *Proc. APS Topical Group on Shock Compression of Condensed Matter*, 2003, in press.
38. D. Ivanov and L. Zhigilei: *Phys. Rev. Lett.*, 2003, vol. 91 (10), p. 5701; *Phys. Rev. B*, 2003, vol. 68 (6), p. 4114.
39. X.W. Zhou, H.N.G. Wadley, R.A. Johnson, D.J. Larson, N. Tabat, A. Cerezo, A.K. Petford-Long, G.D.W. Smith, P.H. Cllifton, R.L. Martens, and T.F. Kelly: *Acta Mater.*, 2001, vol. 49, p. 4005.
40. G. Tas and H.J. Maris: *Phys. Rev. B*, 1994, vol. 49, p. 15046.
41. J.M. McNaney, J. Edwards, R. Becker, T. Lorenz, and B. Remington: *Metall. Mater. Trans. A*, 2004, vol. 35A, pp. 2625-31.
42. M.A. Meyers, D.J. Benson, O. Vohringer, B.K. Kad, Q. Xue, and H.-H. Fu: *Mater. Sci. Eng.*, 2002, vol. A322, p. 194.
43. D.H. Kalantar, A.M. Alien, F. Gregori, B. Kad, M. Kumar, K.T. Lorenz, A. Loveridge, M.A. Meyers, S. Pollaine, B.A. Remington, and J.S. Wark: *Proc. APS SCCM 2001*, AIP, vol. 620, pp. 615-18.
44. L.E. Murr: in *Shock Waves and High-Strain-Rate Phenomena in Metals: Concepts and Applications*, Marc A. Meyers and Lawrence E. Murr, eds., Plenum Press, New York, NY, 1981, pp. 607-73.
45. J.W. Swegle and D.E. Grady: *J. Appl. Phys.*, 1983, vol. 58, p. 941.

46. A. Loveridge-Smith, A. Allen, J. Belak, T. Boehly, A. Hauer, B. Holian, D. Kalantar, G. Kyrala, R.W. Lee, P. Lomdahl, M.A. Meyers, D. Paisley, S. Pollaine, B. Remington, D.C. Swift, S. Weber, and J.S. Wark: *Phys. Rev. Lett*., 2001, vol. 86 (11), p. 2349.
47. D.H. Kalantar, J. Belak, E. Bringa, K. Budil, M. Caturla, J. Colvin, M. Kumar, K.T. Lorenz, R.E. Rudd, J. Stolken, A.M. Allen, K. Rosolankova, J.S. Wark, M.A. Meyers, and M. Schneider: *Phys. Plasmas*, 2003, vol. 10, p. 1569.
48. D.C. Konningsberger and R. Prins: *X-ray Absorption: Principles, Applications, Techniques of EXAFS, SEXAFS, and XANES*, John Wiley & Sons, New York, NY, 1988.
49. P.A. Lee, P.H. Citrin, P. Eisenberger, and B.M. Kincaid: *Rev. Mod. Phys*., 1981, vol. 53, p. 769.
50. J. Rehr and R.C. Albers: *Rev. Mod. Phys*., 2000, vol. 72, p. 621.
51. B. Yaakobi, F.J. Marshall, T.R. Boehly, R.P.J. Town, and D.D. Meyerhofer: *J. Optical Soc. America B–Optical Physics*, 2003, vol. 20, p. 238.
52. B. Yaakobi, D.D. Meyerhofer, T.R. Boehly, J.J. Rehr, R.C. Albers, B.A. Remington, and S. Pollaine: *Phys. Rev. Lett*., 2004, in press.
53. B. Yaakobi, D.D. Meyerhofer, T.R. Boehly, J.J. Rehr, B.A. Remington, P.G. Allen, S. Pollaine, and R.C. Albers: *Phys. Plasmas*, 2004, in press.
54. E.D. Crozier and A.J. Seary: *Can. J. Phys*., 1980, vol. 58, p. 1388.